ARTICLE IN PRESS
OREGEO-01364; No of Pages 22

Ore Geology Reviews xxx (2014) xxx–xxx

Contents lists available at ScienceDirect

Ore Geology Reviews

journal homepage: www.elsevier.com/locate/oregeorev

The Vilalba gold district, a new discovery in the Variscan terranes of the NW of Spain: A geologic, fluid inclusion and stable isotope study

I. Martínez-Abad *, A. Cepedal, D. Arias, A. Martín-Izard

Department of Geology, Oviedo University, C/Arias de Velasco s/n, E-33005 Oviedo, Spain

ARTICLE INFO

Article history:
Received 22 May 2014
Received in revised form 22 October 2014
Accepted 23 October 2014
Available online xxxx

Keywords:
NW Iberian Massif
Gold
Fluid inclusions
Sulfur isotope geochemistry
Intrusion-related gold systems
W–Au skarn

ABSTRACT

This work defines the Vilalba gold district, a new gold region in the NW of Spain comprising three mineralized areas (Castro de Rei, Valiña–Azúmara and Arcos) and two different types of mineralization: 1) W–Au skarn in Castro de Rei, and 2) Au–As (Ag–Pb–Zn–Cu–Sb) vein/disseminated mineralization in Valiña–Azúmara and Arcos. Mineralization is mainly hosted by impure limestone and black slates (lower Cambrian) and spatially related to Variscan and Late-Variscan structures. Rhyolite dikes occur in Arcos (299 ± 6 Ma) and Castro de Rei, both consisting of peraluminous, high-potassium and calc-alkaline rocks. These dikes represent the fractionated expression of unexposed post-tectonic granitoids located at depth. The Castro de Rei area exhibits a contact aureole with biotite ± cordierite and calc-silicate hornfels. Prograde skarn consists of garnet, pyroxene, quartz, wollastonite and scheelite. The retrograde alteration took place in two stages and mainly consists of amphibole, epidote, zoisite, quartz, calcite, chlorite and sulfides. Gold mineralization in the skarn occurs as invisible gold in sulfoarsenides and as electrum related to Bi–Te–S minerals. The mineralization of Valiña–Azúmara and Arcos comprises two stages. The first consists of As-rich pyrite and arsenopyrite with invisible gold. The second stage mainly consists of base metal sulfides and Ag–Pb–Zn–Cu–Sb sulfosalts.

Hydrothermal fluids involved in the skarn formation are low salinity (up to 6.6 wt.% NaCl eq.) aqueous carbonic fluids ($H_2O + CO_2 \pm CH_4 \pm N_2$) evolving into aqueous fluids during the last stage of gold mineralization. Stable isotope geochemistry indicates the importance of a magmatic fluid in the early stages ($\delta^{18}O_{SMOW}$ from 7.5 to 11‰; $\delta^{34}S_{CDT}$ from 2.7 to 5.9‰) that evolved through interaction with host-rocks and mixing with metamorphic and/or meteoric fluids. The $\delta^{34}S_{CDT}$ values (7.8–10.9‰) of second retrograde stage sulfides suggest the incorporation of ^{34}S-enriched from host-rocks. In Valiña–Azúmara and Arcos, the fluid inclusion and isotope studies indicate similar hydrothermal fluids to those associated with the second retrograde skarn stage. Taking into account the fluid inclusion study and mineral geothermometry, an attempt was made to determine the P–T conditions of ore formation. The prograde skarn of Castro de Rei formed at temperatures and pressures ranging from 520 to 560 °C and from 1.7 to 2.5 kb. The mineralization of Valiña–Azúmara formed at minimum P–T conditions of 1.7 kb and 355 °C. The estimated temperatures for the Arcos mineralization are similar to those of Valiña–Azúmara (up to 383 °C) but at lower pressures.

We propose the model of intrusion related gold systems (IRGSs) to explain the mineralizations of the Vilalba gold district. In this model, the Castro de Rei skarn and the Valiña–Azúmara mineralization represent a proximal and a distal deposit, respectively, relative to an unexposed granitoid situated at depth. We also consider Arcos as a distal deposit in relation to another unexposed granitoid located further south in the district.

1. Introduction

The Iberian Variscan Massif (Fig. 1a) is the largest outcrop of pre-Permian rocks within the Iberian Peninsula and constitutes the westernmost exposure of the European Variscides. The northwest of the Iberian Massif has been divided into four zones as follows (Farias et al., 1987; Julivert et al., 1972; Pérez-Estaún et al., 1990). The autochthonous Central-Iberian Zone (CIZ), the allochthonous Galicia–Tras os Montes Zone (GTMZ) and the West Asturian–Leonese Zone (WALZ) represent the hinterland areas; the Cantabrian Zone (CZ) represents the foreland thrust belt (Fig. 1a,b).

The presence of gold in the NW of Spain has been recognized since Roman times. Thus far, several gold mineralized deposits have been defined in this part of the Iberian Massif. They are grouped in the gold belts of Río Narcea, Navelgas, Oscos and Malpica (Spiering et al., 2000), and the gold districts of Salamón (Crespo et al., 2000) and Llamas de Cabrera (Gómez-Fernández et al., 2012) (Fig. 1b). Diverse types of hydrothermal gold deposits have been identified in these gold regions, including different types of skarn (e.g. Carlés, Arcos et al., 1995;

* Corresponding author. Tel.: +34 985105774; fax: +34 985103103.
E-mail address: iker@geol.uniovi.es (I. Martínez-Abad).

http://dx.doi.org/10.1016/j.oregeorev.2014.10.021
0169-1368/

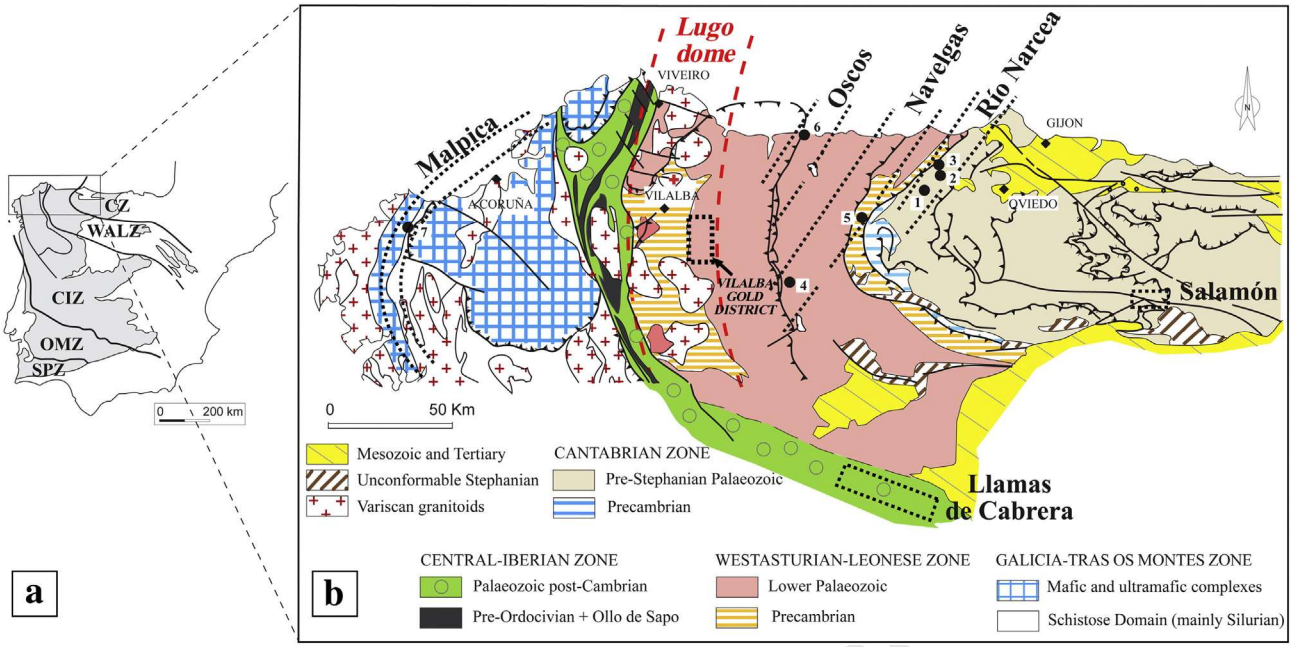

Fig. 1. a) The Iberian Massif. CZ: Cantabrian Zone, WALZ: West Asturian Leonese Zone, CIZ: Central Iberian Zone, OMZ: Ossa Morena Zone, and SPZ: South Portuguese Zone. b) Regional geology of the NW of Spain showing the gold belts (Río Narcea, Navelgas, Oscos and Malpica) defined by Spiering et al. (2000) and gold districts of Salamón (Crespo et al., 2000) and Llamas de Cabrera (Gómez-Fernández et al., 2012). The situation of Vilalba gold district and most important gold deposits is also included: (1) El Valle-Boinás, (2) Carlés, (3) Ortosa, (4) Ibias (5) Linares, (6) Salave, and (7) Corcoesto.

Martín-Izard et al., 2000a; El Valle-Boinás, Cepedal, 2001; Cepedal et al., 2000; Cepedal et al., 2003; Ortosa, Fuertes-Fuente et al., 2000), Carlin-like deposits (e.g. Salamón; El Valle, Cepedal et al., 2008), orogenic gold (Corcoesto, Boiron et al., 1996, 2003; Boixet et al., 2007; Llamas de Cabrera) and intrusion-related gold systems (Linares, Cepedal et al., 2013). The nature and genesis of some other gold deposits in the region, such as the Salave deposit (Fig. 1b), are still not well understood (Fernández-Catuxo, 1998; Gumiel et al., 2008; Harris, 1980a, b; Lang and Baker, 2001; Rodríguez-Terente, 2007). Most of these gold deposits are genetically and/or spatially associated with post-tectonic igneous rocks in addition to the NW–SE, NE–SW, E–W and N–S fracture systems that affected the Iberian Massif during the Late-Variscan.

In this work we report on three gold mineralized areas located between the westernmost gold belts of Oscos and Malpica, near the town of Vilalba (Lugo), constituting a new gold district in NW Spain, the Vilalba gold district (Figs. 1b, 2a). These areas are known from N to S as Castro de Rei, Valiña–Azúmara and Arcos and they are situated in a narrow NNW–SSE oriented, 15 km long zone (Fig. 2a). The mineralization of Valiña–Azúmara was recognized by Schulz in 1835. Later, González Lodeiro et al. (1982) made a first description of the ore, identifying löllingite, jamesonite, galena, tetrahedrite, pyrite and chalcopyrite. Both Castro de Rei, which consists of a W/Au skarn, and Arcos, which consists of a polymetallic deposit similar to Valiña–Azúmara, were discovered during exploration started in 1998 by the Outokumptu company. Both of these occurrences were hitherto unknown. From 1998 to 2004, the last year in a joint venture with Río Narcea Gold Mines, 56 drill holes totalling more than 11,500 m of drilling distributed throughout the three mineralized areas were carried out. These works enabled us to recognize igneous rocks within or close to the mineralized areas. The outcrop of a porphyritic dike in Castro de Rei was previously the only igneous rock known in the area (González Lodeiro et al., 1979).

This paper describes the Vilalba gold district mineralization, characterizes the hydrothermal ore-forming fluids by means of a detailed fluid inclusion study, provides information on possible sources of mineralizing fluids and materials thanks to a stable isotope systematics, reconstructs the P–T conditions of formation of the deposits and proposes a possible metalogenetic model for the district. Moreover, it provides a detailed petrographical and geochemical description of the igneous rocks recognized during the exploration in the district and includes the first geochronological data obtained in these rocks by U–Th–Pb EMPA chemical dating of monazite.

2. Regional geology

The Vilalba gold district is situated in the Mondoñedo Domain (Bastida et al., 1986) of the West Asturian Leonese Zone (WALZ) (Fig. 1b). This domain comprises a thick preorogenic sequence that includes almost all of the Cambrian, Ordovician and Silurian. This sequence lies unconformably upon turbiditic terrigenous sediments of the Villalba Series, which is Upper-Proterozoic in age. The WALZ was affected by three coaxial deformation phases related to a roughly E–W shortening (Martínez-Catalán et al., 1990). The first (D_1) produced large recumbent and overturned folds and a generalized slaty cleavage (S_1). The second (D_2) was responsible for thrust-type structures and associated shear zones. The third (D_3) gave rise to large open folds, approximately homoaxial with the D_1 folds, and also crenulation cleavage (S_3), intense fracturing and shear zones. Regional metamorphic grade increases towards the west, from greenschist to amphibolite facies. During the Late-Variscan NE–SW, NW–SE, E–W and N–S trending fault systems dissected the NW of the Iberian Peninsula (Capote, 1983).

Variscan granitoids are abundant in the western part of the WALZ (Fig. 1b). They are grouped in a N–S trending thermal metamorphic belt called the Lugo Dome (Fig. 1b). The granitoids can be divided into two main groups: syntectonic and post-tectonic (Bellido Mulas et al., 1987; Capdevila et al., 1973; Corretgé et al., 1990, 2004). The syntectonic association is formed by: 1 — tonalite–granodiorite–monzogranite intrusions with features typical of I-Type, calc-alkaline granitoids, that intruded before or syn-cinematically with D_2 and 2 — aluminous leucogranites with features typical of S-type granitoids, which intruded syn-cinematically with D_2. The post-tectonic association is mainly formed by granodiorite–monzogranite intrusions. These

Please cite this article as: Martínez-Abad, I., et al., The Vilalba gold district, a new discovery in the Variscan terranes of the NW of Spain: A geologic, fluid inclusion and stable isotope study, Ore Geol. Rev. (2014), http://dx.doi.org/10.1016/j.oregeorev.2014.10.021

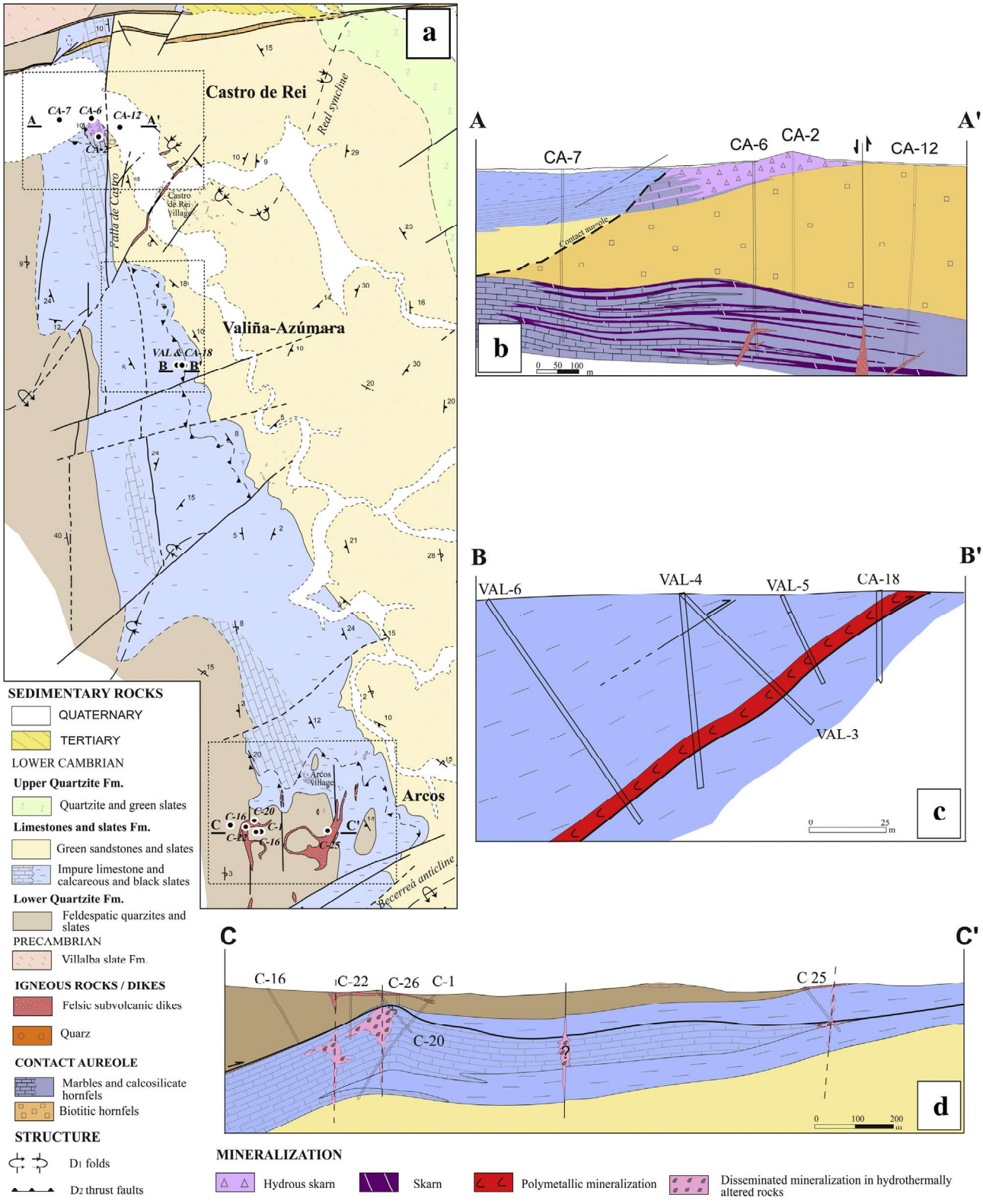

Fig. 2. a) Geological map of the Vilalba gold district. b) A–A′ cross section of the Castro de Rei area. c) B–B′ cross section of the Valiña–Azúmara area. d) C–C′ cross section of the Arcos area.

rocks display features typical of I-Type, high-K, calc-alkaline granitoids. Moreover, they are normally surrounded by contact metamorphism aureoles with paragenesis characteristics of the pyroxene and hornblende hornfels facies developed at estimated pressures of up to 2 kb (Bellido Mulas et al., 1987; Dallmeyer et al., 1997). The Late-Variscan faults formed preferential sites for the emplacement of the post-tectonic intrusions (Corretgé and Suárez, 1990; Gutiérrez Claverol et al., 1991; Martín Izard et al., 2000b; Spiering et al., 2000). The most differentiated facies of the post-tectonic rocks are mainly porphyritic microgranites and leucogranites with biotite, muscovite, garnet and/or tourmaline. They occur in stocks and dikes cutting through the previous igneous rocks and the country rocks. The REE spectra of these differentiated

Please cite this article as: Martínez-Abad, I., et al., The Vilalba gold district, a new discovery in the Variscan terranes of the NW of Spain: A geologic, fluid inclusion and stable isotope study, Ore Geol. Rev. (2014), http://dx.doi.org/10.1016/j.oregeorev.2014.10.021

granitoids are characterized by negative Eu anomalies and a ratio $(Ce/Yb)_N$ between 11.5 and 8 that decreases through the most differentiated facies (Corretgé et al., 2004).

The published U–Pb dating of the Variscan granitoids from the WALZ indicates an age of 325 Ma for the syntectonic calc-alkaline intrusions, 320–310 Ma for the syntectonic aluminous leucogranite intrusions and 300–290 Ma for the post-tectonic calc-alkaline intrusions (Fernández-Suárez et al., 2000; Gutiérrez-Alonso et al., 2011).

3. Sampling and analytical methods

Samples were taken from outcrops and drill cores from the different mineralized areas of the district for mineralogical and petrographical studies and for geochemical analyses. These samples were studied by transmitted and/or reflected-light microscopy, SEM-EDS and EPM (Cameca SX100) at Oviedo University (Spain). In all electron microprobe analyses, the standard deviation of results is less than 0.1%. Major and minor elements were determined at 20 kV accelerating potential, 20 nA beam current and an acquisition time of between 10 and 20 s for X-ray peak and background. In the whole rock samples, major and minor elements were analyzed by inductively coupled plasma emission spectrometry (ICP-ES) and inductively coupled plasma-mass spectrometry (ICP-MS). All the rock analyses were performed in the ACME Analytical Laboratories Ltd. (Canada).

The EMPA chemical dating of monazite (Montel et al., 1996; Suzuki and Adachi, 1991) was done with the Cameca SX100 electron microprobe at the University of Oviedo (Spain) using polished grain mounts. The analyses followed the protocols of Scherrer et al. (2000) for the analysis of U, Th, Pb and rare earth elements (REE), in addition to Si, P, Y, Al and Ca. The chemical age calculations were done with the program provided with the Cameca SX100 geochronology option, which is based on Williams et al. (1999), and Montel et al. (1996), and with the procedure of Cocherie and Albarede (2001). The error in each age determination is reported at the 2-sigma level. To assure quality control we have used a home-made monazite standard with a U–Pb ID-TIMS age of 1083 ± 1 Ma (Valverde-Vaquero et al., 2005) and we have dated the Jefferson Mountain (370 ± 15 Ma EMP age) and the Iveland (951 ± 33 Ma EMP age) monazite standards, for further details see Fernández González et al. (2009). Cumulative plots and weighted average ages were done with Isoplot 3.0 (Ludwig, 2003).

Microthermometric studies were performed on double-polished, 100–300 mm thick plates using a Linkan THMS600 heating-freezing stage at the Ore-deposit Laboratory of the Geology Department (Oviedo University, Spain). The stage was calibrated with melting point standards at $T > 25$ °C and synthetic fluid inclusions at $T < 0$ °C. Measurements of phase changes at or below 31 °C are accurate to within ±0.2 °C and high temperature measurements to within ±2.0 °C. The volumetric fraction of the aqueous phase (flw) was visually estimated by reference to the standard charts of Roedder (1984) and Shepherd et al. (1985). Molar fractions of CO_2, CH_4, H_2S and N_2 were determined in individual fluid inclusions by micro-Raman analysis performed with a Labram Raman spectrometer at CREGU (Nancy, France). Bulk composition and molar volume were computed from P–V–T–X properties of individual fluid inclusions in the C–O–H–S system (Bakker, 1997; Dubessy, 1984; Dubessy et al., 1989; Thiery et al., 1994). The analyses for the stable isotope geochemistry were performed at the Stable Isotopes Laboratory of Salamanca University.

4. Geology of the Vilalba gold district

The rocks exposed in the district are Precambrian, Lower Cambrian and Cenozoic. The Precambrian Villalba Schist (Capdevila, 1969) comprises metasediments and metavolcanic rocks. The Lower-Cambrian succession, which rests unconformably over the Precambrian rocks, is the Cándana Group (Walter, 1966), which includes the Lower Quartzite Formation, the Limestone and Slate Formation and the Upper Quartzite Formation (Fig. 2a). The Limestone and Slate Fm. can also be divided into two members. The lower member, 150 m in thickness, is made up of impure limestone with intercalated layers of calcareous and black slates, and changes laterally to a slate-predominant sequence. The upper member is formed by green sandstones and slates. The mineralization in the district is preferentially hosted in the carbonate-rich lower member. At the north of the district there are tertiary rocks (Miocene in age) located in the tertiary basin of Vilalba (Fig. 2a), which is delimited by E–W faults. Alluvial Quaternary rocks fill the alluvial plain of the Azúmara river. The pre-orogenic stratigraphic sequence is affected by the Variscan regional metamorphism in the facies of the biotite. According to Suárez et al. (1990), in this sector of the WALZ the regional metamorphism [chlorite–biotite–garnet–staurolite (Kyanite) isograds] reached its climax at the end of D_1 or between D_1 and D_2.

The structure of the district is dominated by the overturned Real syncline and Becerreá anticline (Fig. 2a) developed during the first Variscan deformation phase (D_1) and shows a well-developed slaty cleavage. During the (D_2) and (D_3) phases, the overturned folds were affected by thrust faults and sub-vertical folds, respectively. During the Late-Variscan, N–S, E–W and NE–SW trending fault systems dissected the area (Fig. 2a).

The structure of the *Castro de Rei* area is dominated by the overturned Real syncline (D_1), which is affected by a thrust-fault (D_2), a subvertical syncline (D_3) and Late-Variscan faults such as the subvertical N–S Castro fault and NE–SW trending faults. The latter dip from 45° to 55° towards the NW (Fig. 2a,b). The core of the syncline comprises the Limestone and Slate Fm., whereas the outer part comprises the lower Quartzite Fm. In this area, the regional metamorphism (end of D_1 or between D_1 and D_2) was overprinted by a contact metamorphism (post D_3) which produced pyroxene-bearing marble and converted the slates into biotite ± cordierite hornfels. In addition, calcosilicate hornfels developed at the contact between siliciclastic and carbonate rocks and in the levels of calcareous slates. The calcosilicate hornfels consists of pyroxene and plagioclase, with titanite and fluorapatite as accessory minerals. The mineral assemblages of the contact metamorphic rocks from Castro de Rei indicate conditions of hornblende-hornfels facies (Winkler, 1979). This medium-grade metamorphism is similar to that associated with the calc-alkaline post-tectonic granitoids intruded in the Lugo Dome within the Mondoñedo Domain, with estimated maximum pressures of 2 kb (Bellido Mulas et al., 1987; Dallmeyer et al., 1997). Taking this into account, the conditions for the contact metamorphism in Castro de Rei have been estimated to lie within a temperature range of between 520 and 560 °C at a pressure of 2 kb (Winkler, 1979).

The *Valiña–Azúmara* area is located outside of the contact aureole. The main mineralized structure in this area consists of a N–S trending (dip direction from 247° to 261°) thrust fault (D_2) dipping 35° to the west (Fig. 2c). Although less common, in this area the mineralization also occurs filling Late-Variscan N–S subvertical faults and NE–SW faults dipping 55° to the NW. All these structures occur crosscutting black slates from the lower member of the Limestone and Slate Fm.

The structure of the *Arcos* area is dominated by the inverted flank of the overturned anticline of Becerreá (D_1), which is affected by a thrust fault (D_2) and open subvertical folds (D_3). Four major and near vertical Late-Variscan N–S faults dissect the area from east to west (Fig. 2d). The Limestone and Slate Fm. comprises the core of the anticline whereas the Lower Quartzite Fm. comprises the outer part of the fold.

4.1. Igneous rocks

As previously discussed, there are no plutonic rocks outcropping in the Vilalba district, nor was any plutonic body intersected during drilling. The only igneous bodies identified in the district are dikes of subvolcanic rocks found in the areas of Arcos and Castro de Rei during the mining exploration. They intruded along N–S and NE–SW

Please cite this article as: Martínez-Abad, I., et al., The Vilalba gold district, a new discovery in the Variscan terranes of the NW of Spain: A geologic, fluid inclusion and stable isotope study, Ore Geol. Rev. (2014), http://dx.doi.org/10.1016/j.oregeorev.2014.10.021

Late-Variscan faults (Fig. 2), dipping from 55° to near vertical with variable thickness (up to 7 m). In Arcos, they also intruded along bedding planes and D_2 thrust faults in sill-like apophyses. The subvolcanic rocks are mainly felsic, although mafic subvolcanic rocks were also found in Castro de Rei by drilling.

All these subvolcanic rocks normally exhibit slight to pervasive hydrothermal alteration. Sericitization is the most common, although potassic and propylitic alterations were also recognized. Geochemically, there are two types of igneous rock, basaltic andesites and rhyolites (TAS-diagram of Le Maitre et al., 1989, not shown). The basaltic andesites do not seem to be related to the mineralization of the district and show similar characteristics to the NE–SW subvertical basic dikes related to the Cretaceous magmatism in the NW of Spain (Ancochea et al., 1992), although a more detailed study needs to be done.

The rhyolites also comprise two different types of rocks: biotite- and muscovite-bearing rhyolites. The biotite-bearing rhyolites only occur in Castro de Rei. Most of the dikes were found by drilling. Only one dike, trending in the NE–SW direction and dipping 55° towards the NW, crops out to the north of Castro de Rei village (Fig. 2a). The biotite-bearing rhyolite has porphyritic texture and consists of quartz, K-feldspar, plagioclase and biotite phenocrysts (Fig. 3a,b). The groundmass is fine-grained with mosaic or micropoikilitic texture and consists of small and irregular quartz patches enclosing variably oriented, altered feldspar laths (snowflake texture). This texture suggests a devitrification process of cooling glass. Accessory minerals are amphibole, monazite, allanite, apatite and zircon.

The muscovite-bearing rhyolite occurs in the Arcos area mainly associated with N–S faults, although this rock also occurs as sills emplaced in D_2 thrust faults or stratigraphic planes (Fig. 2d). This rock has porphyritic to microgranitic texture, and comprises abundant phenocrysts of quartz, alkali feldspars, slightly or pervasively sericitized, and muscovite (Fig. 3c,d). The groundmass is normally formed by the same minerals and is fine to very fine-grained. In some cases the groundmass of these rocks shows a micropoikilitic texture similar to that observed in the biotite-bearing rhyolite, suggesting a devitrification process of cooling glass. Accessory minerals are biotite, zircon, apatite, monazite and pyrite and arsenopyrite, usually completely oxidized.

4.2. Monazite EMPA dating

We attempted to date the felsic subvolcanic rocks from the Vilalba gold district using the U–Th–Pb EMPA chemical dating method in monazite. The details are described in the Sampling and analytical methods section. Representative analyses of monazite from Arcos and Castro de Rei are presented in Table 1. Both are Ce-rich and show a high concentration of LREE, common in this kind of monazite (Foerster, 1998). The monazite from the biotite-bearing rhyolite occurs as corroded and irregular crystals, with porous cores. This fact prevented us from obtaining enough high quality analyses for their dating. The U–Th–Pb EMPA dating method was only possible for use in monazites from the muscovite-bearing rhyolite. A total of 20 single analyses on 7 individual monazite grains were made, the set of individual ages ranging from 258 to 333 Ma. These ages show a normal distribution, with a weighted average age of 295.9 ± 9.8 Ma (MSWD 0.8) and Th/Pb–U/Pb age of 299 ± 6 Ma (Fig. 4).

4.3. Igneous geochemistry

Samples of the felsic subvolcanic igneous rocks were selected from outcrops and drill-cores. The geochemical results are compiled in Table 2. The analyzed samples from muscovite-bearing dikes appear unaltered. However all the samples from biotite-bearing dikes show signs of hydrothermal alteration.

The recalculated whole-rock analyses for the muscovite-bearing rhyolites show high contents in SiO_2 (73–75.5% wt.%), K_2O (4.2–4.5 wt.%), and Na_2O (3.3–4.6% wt.%) and low contents in FeOt (<1.3 wt.%), MgO (≤0.06 wt.%), CaO (≤0.05 wt.%), P_2O_5 (≤0.12 wt.%) and TiO_2 (0.01 wt.%). The biotite-bearing rhyolites show also high contents in SiO_2 (74.3–76.4% wt.%) and K_2O (3.9–6.3 wt.%), but they show higher TiO_2 and MgO contents (<0.2 wt.% and <0.3 wt.%, respectively) and

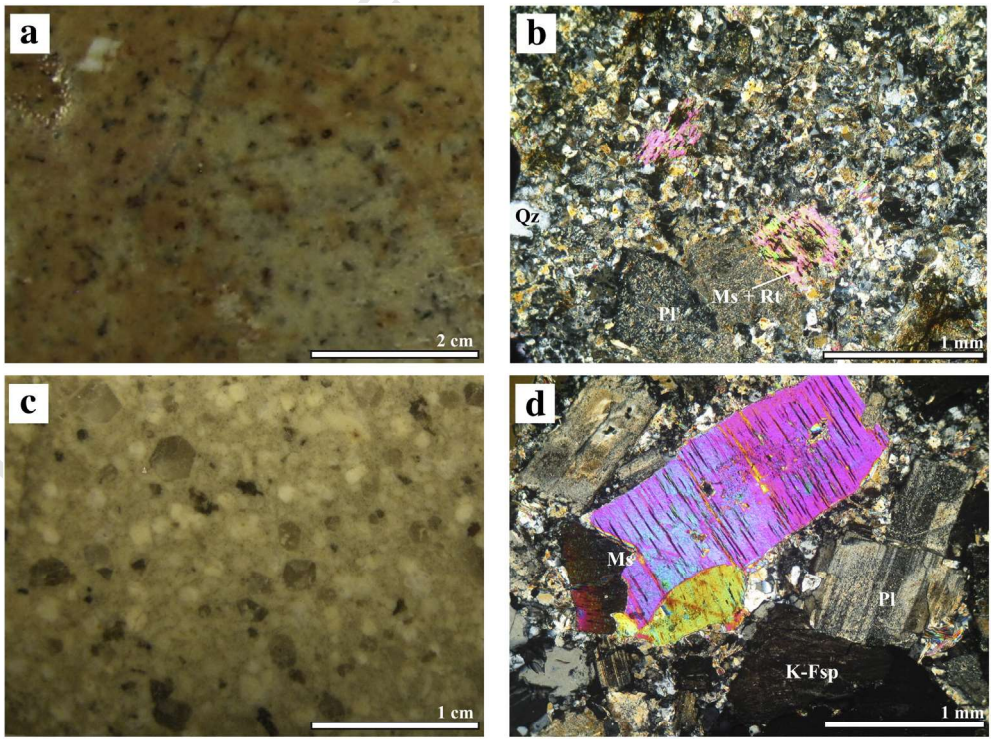

Fig. 3. a) Hand sample of a sericited biotite-bearing rhyolite from Castro de Rei. b) Photomicrograph of the previous sample showing the porphyritic texture of the rock. The plagioclase (Pl) is altered to white mica (microcrystalline variety) and the biotite is altered to muscovite and rutile (Ms + Rt) (CPL). c) Hand sample of a muscovite-bearing rhyolite from Arcos. d) Photomicrograph of the previous sample showing the porphyritic and seriated texture of the rock. The plagioclase is slightly altered to microcrystalline white mica (CPL).

Please cite this article as: Martínez-Abad, I., et al., The Vilalba gold district, a new discovery in the Variscan terranes of the NW of Spain: A geologic, fluid inclusion and stable isotope study, Ore Geol. Rev. (2014), http://dx.doi.org/10.1016/j.oregeorev.2014.10.021

Table 1
Representative electron microprobe analyses of monazites from the muscovite bearing rhyolite and biotite-bearing rhyolite.

	Muscovite-bearing rhyolite			Biotite-bearing rhyolite		
P_2O_5	27.29	25.70	25.53	28.03	28.53	29.83
Al_2O_3	0.00	0.00	0.00	0.00	0.02	0.01
SiO_2	1.36	1.51	2.06	0.95	0.67	0.39
CaO	0.05	0.06	0.04	0.38	0.49	0.42
Y_2O_3	2.61	2.07	2.12	0.42	0.65	0.66
La_2O_3	6.31	6.60	6.14	14.48	14.63	16.07
Ce_2O_3	25.11	26.11	24.84	29.40	30.11	30.07
Pr_2O_3	4.00	3.86	3.72	3.15	3.28	3.18
Nd_2O_3	17.48	15.71	16.33	12.18	12.71	12.10
Sm_2O_3	5.21	4.52	4.43	1.96	2.26	1.77
Gd_2O_3	2.64	2.30	2.27	1.17	1.32	1.00
Tb_2O_3	0.20	0.19	0.20	0.08	0.06	0.07
Dy_2O_3	0.75	0.65	0.66	0.25	0.25	0.24
Ho_2O_3	0.01	0.00	0.02	0.00	0.00	0.00
Er_2O_3	0.10	0.08	0.09	0.01	0.02	0.03
Yb_2O_3	0.00	0.00	0.00	0.00	0.00	0.00
PbO	0.11	0.14	0.16	0.10	0.07	0.05
ThO_2	6.69	10.25	10.68	7.36	5.20	3.87
U_2O_3	0.47	0.47	0.51	0.00	0.01	0.07
Total	100.39	100.19	99.78	99.92	100.26	99.82
P	3.73	3.61	3.58	3.82	3.85	3.97
Al	0.00	0.00	0.00	0.00	0.00	0.00
Si	0.22	0.25	0.34	0.15	0.11	0.06
Ca	0.01	0.01	0.01	0.06	0.08	0.07
Y	0.22	0.18	0.19	0.04	0.05	0.06
La	0.38	0.40	0.38	0.86	0.86	0.93
Ce	1.48	1.59	1.51	1.73	1.76	1.73
Pr	0.24	0.23	0.22	0.18	0.19	0.18
Nd	1.01	0.93	0.97	0.70	0.72	0.68
Sm	0.29	0.26	0.25	0.11	0.12	0.10
Gd	0.14	0.13	0.12	0.06	0.07	0.05
Tb	0.01	0.01	0.01	0.00	0.00	0.00
Er	0.04	0.03	0.04	0.01	0.01	0.01
Dy	0.01	0.00	0.00	0.00	0.00	0.00
Pb	0.00	0.01	0.01	0.00	0.00	0.00
Th	0.25	0.39	0.40	0.27	0.19	0.14
U	0.02	0.02	0.02	0.00	0.00	0.00

lower Na_2O contents (1.9–3.4 wt.%) than the muscovite-bearing ones. All the rocks are calc-alkaline high-K and peraluminous (Fig. 5a,b). The dispersion observed in the biotite-bearing rhyolite values (A/CNK = 1.05–1.5, Fig. 5b) may be due to the hydrothermal alteration that these rocks show.

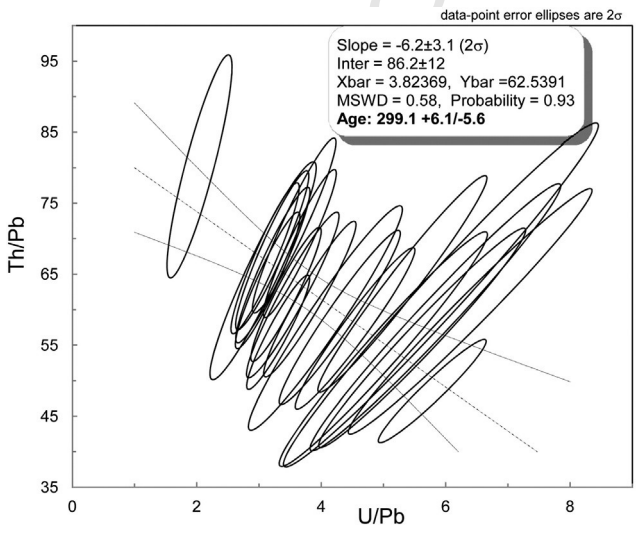

Fig. 4. U–Th–Pb monazite EMPA chemical age, Th/Pb–U/Pb diagram for the muscovite-bearing rhyolite rocks.

Table 2
Geochemical analyses of the felsic subvolcanic rocks from the Vilalba gold district.

Sample	Muscovite-bearing rhyolite				Biotite-bearing rhyolite		
	AR1	AR6	AR7	AR8	C2	C3	C64
Wt.%							
SiO_2	72.28	72.77	70.33	73.49	74.38	75.02	73.00
TiO_2	<0.01	<0.01	<0.01	<0.01	0.18	0.03	0.12
Al_2O_3	16.01	15.26	16.00	14.85	14.28	14.49	13.32
Fe_2O_3	0.65	0.67	0.70	0.79	1.18	0.97	1.31
FeO	0.38	0.42	0.42	0.49	0.24	0.28	0.46
MgO	0.06	0.01	0.04	0.03	0.26	0.09	0.28
MnO	0.07	0.07	0.10	0.09	<0.01	<0.01	0.01
CaO	0.03	0.05	0.03	0.04	0.12	0.13	1.62
Na_2O	4.48	3.91	4.28	3.19	3.29	3.34	1.85
K_2O	4.17	4.4	4.26	4.41	4.48	3.83	6.23
P_2O_5	0.12	0.08	0.10	0.03	0.05	0.04	0.05
H_2O/LOI	2.0	2.6	4.1	3.0	1.6	1.9	2.0
Total	100.25	100.24	100.36	100.41	100.02	100.12	100.25
MALI(1)	8.77	8.46	8.84	7.76	7.77	7.17	6.58
ppm							
Rb	980.3	906.4	965.7	885.8	157.3	115.5	237.9
Ba	26	47	36	16	591	794	648
Sr	13.2	24	14.5	3.4	120.5	136.3	196.4
Cs	15.8	46.1	65.3	40.2	6.9	4.1	8.8
Be	6	51	4	16	2	1	2
Nb	42.9	43.6	36.4	46.7	14.6	13.3	15.4
Ta	16.7	15.5	15	12.4	1.8	1.6	2.1
Zr	20.2	24.8	25.1	22.6	128.8	51.6	114.8
Th	10.7	13.2	11.8	12	16.7	9.2	15.6
Hf	2.7	3	2.8	2.3	4	2.3	3.7
U	10.5	8.9	4.8	11.1	5.6	4.2	8
Y	96.9	81.8	84.4	81	16	10.8	16.8
La	16.6	20.5	14.9	12.4	30.5	16.7	28.8
Ce	60.6	53.1	55.5	48	62	34.4	62
Pr	8.96	10.17	7.64	6.51	6.58	3.66	6.48
Nd	33.8	39.6	27.9	26.2	24	12.7	23.5
Sm	15.36	15.78	12.4	10.26	4.42	2.86	4.29
Eu	0.05	0.03	<0.02	<0.02	0.71	0.54	0.68
Gd	14.74	13.77	12.46	10.44	3.19	2.37	3.32
Tb	3.1	2.81	2.8	2.47	0.53	0.41	0.54
Dy	16.52	14.38	15.15	13.83	2.83	2.12	2.91
Ho	2.59	2.36	2.46	2.36	0.53	0.36	0.54
Er	7.28	6.95	7.01	7.25	1.48	1.06	1.66
Tm	1.18	1.16	1.12	1.3	0.24	0.16	0.23
Yb	8.79	8.36	7.79	10.19	1.56	1.01	1.55
Lu	1.14	1.15	1.05	1.46	0.22	0.15	0.22
(Ce/Yb)	1.79	1.65	1.85	1.22	10.3	8.83	10.37
Eu/Eu*	0.01	0.01	0.005	0.01	0.58	0.63	0.58
Co	55.2	19.5	32.3	39.2	46.7	23.1	27
Ni	<20	21	<20	<20	<20	<20	<20
Sc	3	5	3	7	4	2	3
V	17	<8	<8	<8	9	<8	<8
Cu	0.7	0.9	0.9	0.9	2.1	5.2	70.6
Pb	9.4	7.8	5.7	13.3	3.6	13	7.3
Zn	43	30	27	27	3	17	5
Bi	7.4	6.6	0.7	7	0.3	0.2	0.3
Sn	81	56	35	53	6	4	9
W	441.8	135.8	118.9	257.9	341.3	174.5	354.7
Mo	<0.1	<0.1	<0.1	<0.1	0.1	<0.1	0.5
As	5	11.8	4.1	1.8	157.2	218.3	502.6
Au (ppb)	0.7	<0.5	<0.5	1.1	1	5.6	108.4
Sb	0.8	3.2	0.5	0.6	1.8	4.5	5.7

Taking into account trace elements, the muscovite-bearing rhyolites are characterized by high contents (in ppm) of the alkali metals Rb (≤980.3) and Cs (≤65.3) and of some HFSE such as Y (<97), Nb (≤46.7), and Ta (≤16.7). They have very low Ba (16–47), Sr (3.4–24), Eu (≤0.05) and Zr (20–25) contents (Table 2). These rocks have flat "bird-wing shape" chondrite-normalized REE patterns that are characterized by low $(Ce/Yb)_N$ ratios (from 1.2 to 1.85, Table 2), small negative La and Nd anomalies and pronounced negative Eu anomalies (Eu/Eu* = 0.005–0.01) (Fig. 5c). The biotite-bearing rhyolites have a moderately fractionated pattern with $(Ce/Yb)_N$ ratios from 8.8 to 10.4 and show small Eu anomalies (Eu/Eu* = 0.58–0.63) (Fig. 5c). Both types of

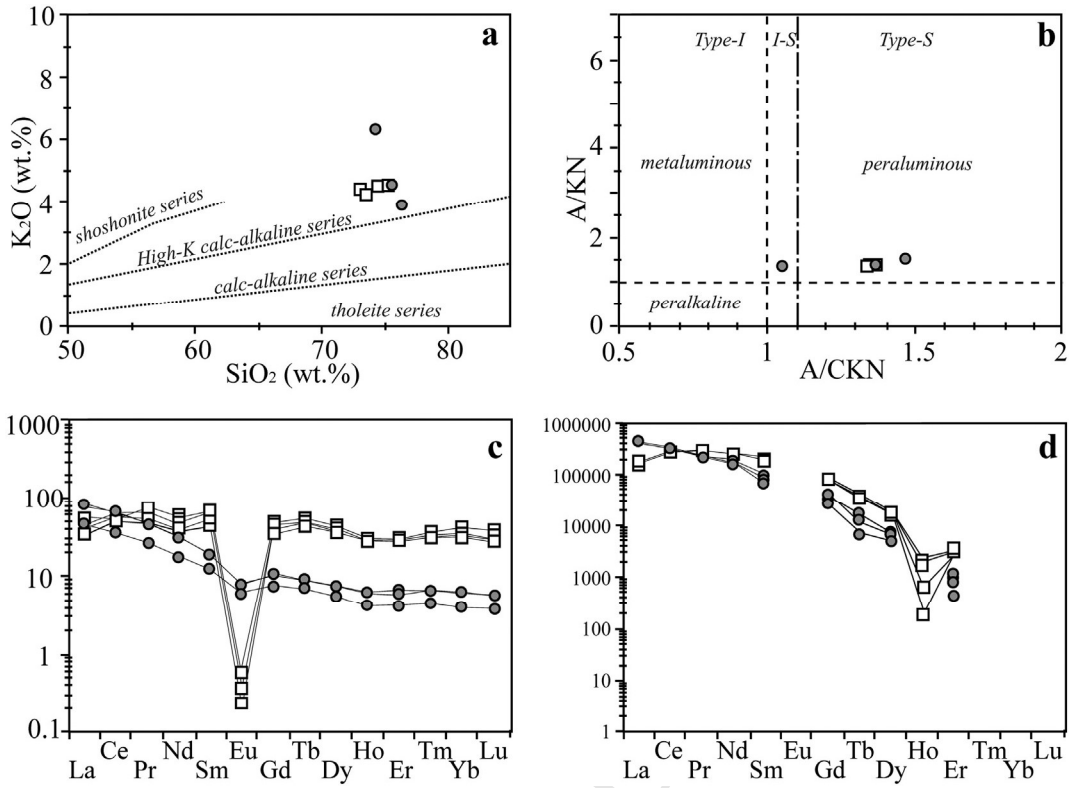

Fig. 5. Recalculated analyses of the felsic subvolcanic rocks present in the district plotted on: a) K_2O vs. SiO_2 binary diagram (Rickwood, 1989). b) A/KN vs. A/CKN binary diagram. c) Chondrite-normalized REE patterns of the igneous rocks. d) Chondrite-normalized REE patterns of the analyzed monazite. Normalizing values are from Taylor and McLennan (1985). White squares: muscovite-bearing rhyolite. Gray circle: biotite-bearing rhyolite.

rhyolite show a similar fractionation of HREE in the normalized patterns, although the muscovite-bearing ones appear enriched in HREE. Fig. 5d shows the chondrite-normalized REE patterns of the analyzed monazite from both types of rhyolite. These patterns reproduce those of the igneous rocks for LREE (La-Sm) and evidence the strong effect that this mineral exerts in the rare earth content of the whole rock.

Villaseca et al. (2004) observed that I and S-type granites from the Central Iberian Zone of the Iberian Massif display contrasting evolutionary patterns for Th, Y and REE. The characteristic P-poor composition of I-type magmas determines the rare early crystallization of phosphates and, thus, favors an increasing richness in those incompatible elements usually incorporated into phosphate accessories (i.e. monazite, xenotime and apatite) in residual magma (Champion and Chappell, 1992; Foerster, 1998). According to Villaseca et al. (2004), trace element contents in accessory phases, such as monazite and xenotime, can be used to discriminate between I and S-type granites. Th, Y and HREE contents in monazite and xenotime are lower in S-type granites compared to those in less peraluminous ones. This is reflected in lower Th/U ratios in monazite and xenotime from S-type granites than from I-type granites. The monazite from the rhyolites of Arcos and Castro de Rei both show Th/U ratios characteristic of I-type granites (Fig. 6).

The differences in the major and trace element composition of both rocks display the characteristic evolutionary pattern of I-type granites. The muscovite-bearing rhyolite would represent a more evolved rock, poorer in Ti, Fe, Mg, Sr, Ba and Eu and richer in incompatible elements such as Sc, Rb, Nb, Ta and HREE with respect to a less evolved biotite-bearing rhyolite.

Taking into account the different granitic rocks that occur within the Lugo Dome of the Mondoñedo Domain, the igneous felsic rocks from the Vilalba gold district show petrological and geochemical characteristics similar to the differentiated facies of the calc-alkaline post-tectonic granitoids (Corretgé et al., 2004), e.g. negative Eu anomalies and small REE fractionation that decrease through the most differentiated facies, the muscovite-bearing rhyolites in this case.

Furthermore, these rocks show no signs of deformation, are intruded along Late-Variscan faults and, in the case of the moscovite-bearing rhyolites, show an absolute age of 299 ± 6 Ma, similar to the calc-alkaline post-tectonic granitoids. Therefore, we consider that these felsic rocks constitute the dike suite of two unexposed post-tectonic granitic rocks situated at depth, one in the area of Arcos and the other in the area of Castro de Rei, where the occurrence of contact aureole hornfels similar to that developed in other post-tectonic granitoids of the Lugo Dome

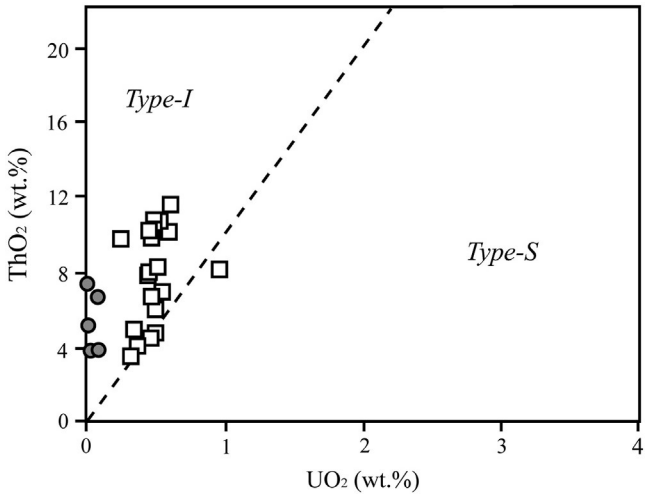

Fig. 6. ThO_2 vs. UO_2 plot of monazite from the felsic subvolcanic rocks present in the district. The dashed line separates the ThO_2/UO_2 composition fields that are assigned to the I-type and S-type granites. White squares: muscovite-bearing rhyolite. Gray circle: biotite-bearing rhyolite.

Please cite this article as: Martínez-Abad, I., et al., The Vilalba gold district, a new discovery in the Variscan terranes of the NW of Spain: A geologic, fluid inclusion and stable isotope study, Ore Geol. Rev. (2014), http://dx.doi.org/10.1016/j.oregeorev.2014.10.021

and the skarn mineralization evidences the presence of an unexposed granitic body (Fig. 2a,b).

5. Mineral deposits

Two main types of mineral deposit can be distinguished within the district: a W–Au skarn in Castro de Rei and polymetallic vein/disseminated deposits in Valiña–Azúmara and Arcos.

5.1. W–Au skarn of Castro de Rei

The skarn-type mineralization developed in the Castro de Rei area was mainly controlled by the Castro fault (Fig. 2b), and spreads laterally through both flanks of the syncline along bedding and cleavage planes, thereby affecting receptive facies of the lower member of the Limestone and Slate Fm. The alteration produced several levels of calcic skarn with variable thickness. The prograde skarn mainly consists of garnet (Adr_{23-59}), pyroxene (Hd_{34-96}) and quartz, with lesser amounts of scheelite, K-feldspar and fluorapatite (Fig. 7a,b; Table 3). The garnet/pyroxene ratio is about 60/40 in the proximal zones of the skarn, and decreases towards the distal zones, where the skarn is made up of pyroxene and quartz at the marble contact. Locally, wollastonite occurs at the contact between the garnet-bearing skarn and marble (Martinez-Abad et al., 2011a). Some of the microprobe analyses were performed on garnet shown spessartine + almandine proportions above 5% (up to 10%), suggesting that they are subcalcic (Newberry, 1983). The retrograde skarn alteration processes affected not only the prograde skarn but also the calc-silicate hornfels and marble, developing a "hydrous skarn" mostly in the inverted flank of the syncline (Fig. 2b). The retrograde skarn alteration can be divided into two stages. During the first stage, the alteration of the prograde skarn produced amphibole, epidote, quartz (Qz1), calcite (Cal1), titanite and sulfides (Fig. 7c; Table 3). The alteration of the calc-silicate hornfels produced amphibole, zoisite, K-feldspar, quartz (Qz1) and calcite (Cal1). Sulfides associated with the first stage of retroskarn are mainly pyrrhotite, with arsenopyrite (Apy I), chalcopyrite, sphalerite, molibdenite and cobaltite as accessory minerals (Martinez-Abad et al., 2011a).

The second stage of retroskarn can be divided into two phases. The first consists of quartz (Qz2), calcite (Cal2), sericite–muscovite, together with arsenopyrite (Apy II) and pyrite with variable amounts of As (Table 3). During this phase, a locally intense carbonatization of the host rocks took place, in addition to the destabilization of the early pyrrhotite to pyrite and marcasite. The second phase consists of chlorite, prehnite, quartz (Qz3), calcite (Cal3), base metal sulfides, Bi–Te–S minerals (native-Bi, hedleyite, joséite-B and bismuthinite) along with sulfides and sulfosalts of Bi–Ag–Sb–Cu–Pb (Table 3). Gold is associated with the second stage of retrograde skarn and occurs as "invisible gold" in As-rich pyrite and arsenopyrite or as electrum (19 to 15 wt.% Ag) associated with the Bi–Te–S minerals (Fig. 7d). This is reflected by the strong Au–Bi correlation observed in the drill core assay results ($R^2 = 0.9$).

According to the EMPA data, the Apy1 presents As values ranging from 32.5 to 33.9 at.% As. Arsenopyrite from the second stage of retrograde alteration processes (Apy2) shows a composition varying from 30.8 to 35.8 at.% As. Under scanning electron microscopy, the Apy2 crystals appear zoned with As-rich rims (>33 at.% As) and cores ranging from 30.8 to 31.5 at.% As. Some of the microprobe analyses in the As-rich rims show traces in Au (up to 410 ppm) and impurities in Sb (≤0.46 wt.%). Moreover, the EMPA carried out in pyrite associated with Apy2 indicates amounts of As up to 2.6 wt.%. The BSE images of these crystals also revealed zonation in composition consisting of As-poor cores and As-rich rims, the latter also with detectable Au (up to 380 ppm).

5.2. The polymetallic vein/disseminated mineralization

This type of mineralization is present in the areas of Valiña–Azúmara and Arcos. In Valiña–Azúmara, the mineralization occurs cementing D_2 thrust fault breccias and forming hydrothermal veins that seal fractures from the N–S and the NE–SW fault systems. All these structures

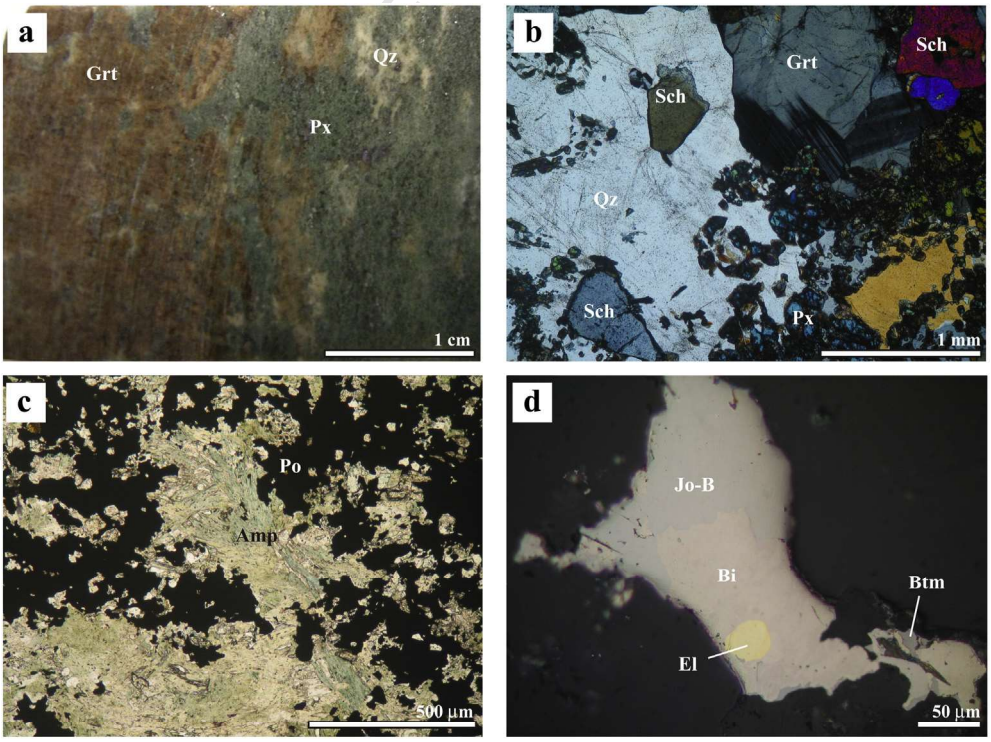

Fig. 7. a) Hand sample of the garnet–pyroxene–quartz prograde skarn. Grt: garnet; Px: piroxene; Qz: quartz. b) Photomicrograph of the previous sample showing disseminated grains of scheelite (Sch) (CPL). c) Photomicrograph that shows amphibole (Amp) intergrowths with pyrrhotite (Po) from the first stage of the retrograde alteration of the skarn (CPL). d) Aggregate of native-Bi (Bi), joséite-B (Jo-B), electrum (El) and bismuthinite (Btm).

Please cite this article as: Martínez-Abad, I., et al., The Vilalba gold district, a new discovery in the Variscan terranes of the NW of Spain: A geologic, fluid inclusion and stable isotope study, Ore Geol. Rev. (2014), http://dx.doi.org/10.1016/j.oregeorev.2014.10.021

t3.1 **Table 3**
t3.2 Summary of the relationships between the episodes of mineralization, mineral assemblages and hydrothermal fluids in the mineral deposits of the Vilalba gold district.

t3.3 Deposit	Episode of mineralization	Typical mineral assemblage	Hydrothermal alterations	Fluid type and composition
t3.4 Castro de Rei	Prograde skarn	Grt, Px, Qz, Cal, Wo, Sch	Metasomatism of metasedimentary host-rocks	H_2O–NaCl–CH_4–(CO_2–N_2) [*Lw-(cm)*; *VLcm-w*]
t3.5	1st stage of retroskarn	Amp, Ep, Zo, Qz1, Cal1, Po, Apy1, Ccp, Mol	Amphibolitization ± epidotization	No fluid inclusions studied
t3.6 t3.7	2nd stage of retroskarn 1st phase	Qz2, Cal2, Ms, Apy2, Py, Mrc	Phyllic alteration, carbonatization	H_2O–NaCl–CO_2 [*VLc-w*]
t3.8	2nd phase	Chl, Prh, Qz3, Cal3, Bi–Te–S minerals, Bi–Ag–Sb–Cu–Pb minerals	Chloritization	H_2O–NaCl [*Lw*, *Lw-s*]
t3.9 Valiña–Azúmara	1st stage (Au–As)	Qz, Cal, Py, Apy	Phyllic alteration, silicification	H_2O–NaCl–CH_4–CO_2–N_2 [*VLcm-w1*; *VLcm-w2*]
t3.10	2nd stage (Ag–Pb–Zn–Cu–Sb)	Cal I, Qz I, Chl, Sph, Gn, Ccp, Ttr, Jm	Not observed	H_2O–NaCl [*Lw*]
t3.11 Arcos	1st stage (Au, As)	Qz, Ca–Mg–Fe Cb, Py, Apy	Phyllic alteration, silicification, dolomitization	H_2O–NaCl–CO_2–(CH_4) [*Lw-(cm)*; *Lw-(c)*]
t3.12 Q7	2nd stage (Ag–Pb–Zn–Cu–Sb)	Ca–Mg–Fe Cb, Qz I, Chl, Fl, Po, Ccp, Sph, Gn, Ttr, Bi–Pb–Sb sulfosalts	Not observed	H_2O–CO_2 [*Lw-c*, *Lw?*]

t3.13 Grt: garnet, Px: piroxene, Qz: quartz, Cal: calcite, Wo: wollastonite; Sch: scheellite; Amp: amphibole, Ep: epidote, Zo: zoisite, Po: pyrrothite, Apy: arsenopyrite, Ccp: chalcopyrite,
t3.14 Mol: molibdenite, Ms: muscovite, Mrc: marcasite, Chl: chlorite, Prh: prehnite, Sph: sphalerite; Gn: galena, Ttr: tetrahedrite, Jm: jamesonite; Fl: fluorite. In the fluid type and composition
t3.15 column: the first line describes the composition and the second line describes the types of fluid inclusions identified. The notation of fluid inclusion types follows the nomenclature
t3.16 previously published by Cathelineau et al. (1993) and Boiron et al. (1996).

are hosted by calcareous and black slates (Fig. 2c). Moreover, the mineralization also occurs disseminated within narrow weakly silicified and sericitized selvages around these structures (Fig. 8a). In Arcos, the ore mainly occurs disseminated in hydrothermally altered muscovite-bearing rhyolites and sedimentary rocks from the lower member of the Limestone and Slate Fm. To a lesser extent, the ore is also found forming hydrothermal veins sealing fractures from the N–S fault systems (Fig. 2d). The different types of host-rock alteration observed were: sericitization, dolomitization and silicification. The alteration mainly developed along the N–S fault systems and in some cases spreads laterally along D_2 thrust faults and bedding and S_1 cleavage planes. The phyllic alteration occurred on muscovite-bearing rhyolites and black slates whereas the calcareous rocks (impure limestone and calcareous slate) were affected by dolomitization and silicification, the latter developing jasperoids (Fig. 8b).

In both areas, the mineralization was developed in two main stages (Table 3): 1) Au–As; 2) Ag–Pb–Zn–Cu–Sb. The first consists of fine-grained pyrite, As-rich pyrite and arsenopyrite, in a matrix of quartz and/or calcite. Gold occurs as "invisible gold" in the As-rich pyrite and arsenopyrite. Several types of pyrite and arsenopyrite were defined according to their chemical and textural characteristics (Martínez-Abad et al., 2011b). The first type, Py-I, is poor in arsenic and other trace elements and occurs as subhedral grains, sometimes with porous texture. Py-II is rich in As (up to 5 wt.%) and forms fine-grained

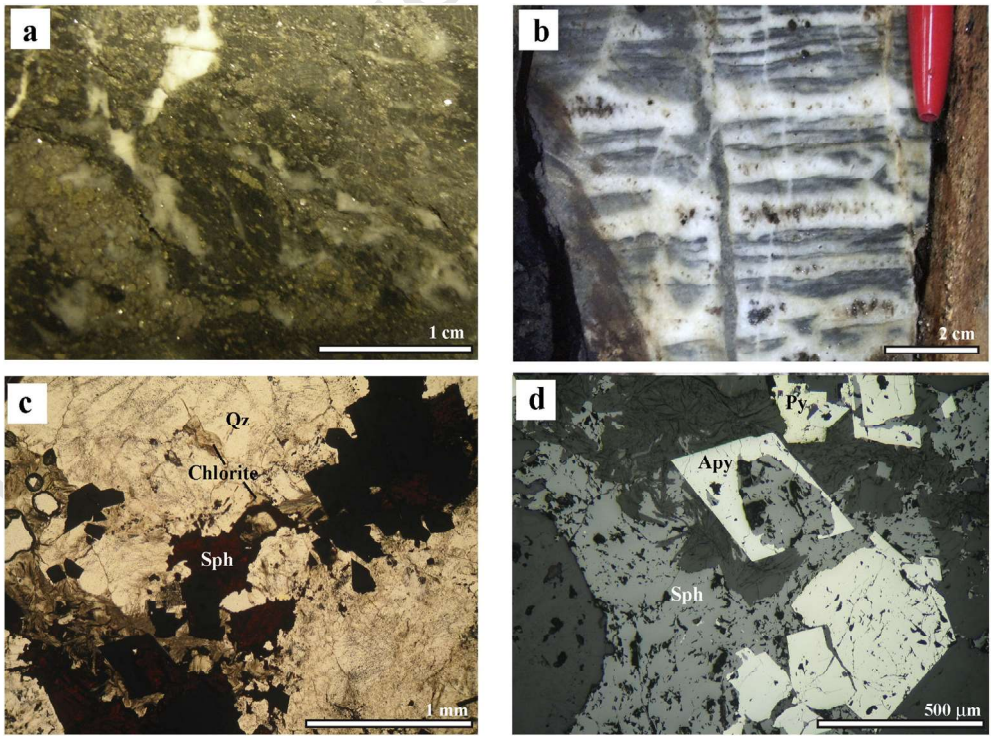

Fig. 8. a) Hand sample of a black slate crossed by quartz-calcite-pyrite-arsenopyrite veinlets with disseminations of pyrite and arsenopyrite. b) Drill core sample of a silicified limestone (jasperoid) from Arcos. c) Photomicrograph of a mineralized vein formed by quartz (Qz), chlorite, sphalerite (Sph) and opaque crystals (pyrite and arsenopyrite) (PPL). d) Photomicrograph of the polymetallic mineralization. It consists of arsenopyrite (Apy) and pyrite (Py) grains from the first stage of mineralization enclosed and partially replaced by sphalerite grains from the second stage of mineralization (RL).

Please cite this article as: Martínez-Abad, I., et al., The Vilalba gold district, a new discovery in the Variscan terranes of the NW of Spain: A geologic, fluid inclusion and stable isotope study, Ore Geol. Rev. (2014), http://dx.doi.org/10.1016/j.oregeorev.2014.10.021

pyritohedra and overgrowth rims in the previously mentioned pyrite. Py-II shows trace contents of Cu, Sb and Au. The highest amounts of Au were measured in the Py-II from the Arcos deposit (>0.2 wt.%) (Martínez-Abad et al., 2011b) whereas, in Valiña–Azúmara, the Au content was always below the detection limit (<250 ppm). A third type of pyrite, Py-III, similar in composition to Py-I, was observed in Arcos, forming a last overgrowth. Moreover, two types of arsenopyrite were defined. The first, Apy-I, appears associated with Py-I and Py-II as coarse grains infilling veins or disseminated in the host-rocks. In Valiña–Azúmara, the Apy-I has a composition ranging between 30.8 and 34.1 at.% of As. In Arcos, this arsenopyrite has a composition varying between 30.2 and 31.5 at.% As, with important amounts of Co (<4.5 wt.%). A second type of arsenopyrite, Apy-II, was only defined in Arcos. It occurs as idiomorphic and small (10 to 200 μm) acicular grains with a composition varying between 28.9 and 33.6 at.% As. The crystals are strongly zoned showing As-poor cores (25.4–28.7 at.%). Gold was only detected in the Apy-II from Arcos (up to 0.03 wt.%) in very few EMPAs (Martínez-Abad et al., 2011b).

The minerals from the second stage replace the early ones (Fig. 8c,d; Table 3), with the addition of quartz, Fe/Mg-rich carbonates, and chlorite or fluorite. The metal assemblage observed depends on the area. In Valiña–Azúmara, it comprises sphalerite, galena, chalcopyrite, Ag-rich tetrahedrite (up to 19 wt.% Ag) and jamesonite. In Arcos, it consists of pyrrhotite, chalcopyrite, sphalerite, galena, Ag-rich tetrahedrite (up to 4 wt.% Ag), electrum (25 to 27 wt.%) and Bi–Pb–Sb sulfosalts.

6. Fluid inclusion study

A fluid inclusion (FI) study was carried out in order to reconstruct the P–T–X evolution of the ore-related fluids. More than three hundred and forty fluid inclusions were examined in samples from the three mineralized areas. Different types of fluid inclusion were defined, taking into account the microscope observations such as the number of phases present at room temperature, vapor/liquid ratios, primary or secondary origin, microthermometric measurements, and Raman analyses of the volatile phase. The notation of fluid inclusion types follows the nomenclature previously published by Cathelineau et al. (1993) and Boiron et al. (1996).

6.1. Fluid inclusions from Castro de Rei

The fluid inclusions study in the skarn of Castro de Rei was performed in quartz and garnet crystals from the prograde skarn as well as in quartz crystals (Qz2) from veins or cavities related to the second retrograde stage that produced the carbonatization and chloritization of the host-rocks (Table 3). However, we did not find FI in minerals from the first stage of retrogradation.

Four different types of fluid inclusion were defined, three of them are aqueous-carbonic [Type-I or Lw-(cm), Type-II or VLcm-w and Type-III or VLc-w], and the other one aqueous (Type-IV or Lw/Lw-s) (Table 3). These types are described below and microthermometric results and Raman analyses of the volatile phase are summarized in Table 4.

6.1.1. Type-I or Lw-(cm)

These FIs were found in garnet and quartz crystals from the prograde skarn (Fig. 9). They are polyhedral or ellipsoidal in shape, their sizes vary between 8 and 24 μm, and occur isolated or in small clusters. On the basis of the criteria of Roedder (1984), these inclusions are interpreted as primary. In some quartz samples, this type of FI may appear associated with the Type-II inclusions (Fig. 9). The inclusions show two phases at room temperature with the volumetric fraction of the aqueous phase (flw) between 0.4 and 0.7. The presence of a volatile component was only detected through the clathrate formation (Table 4). Where it was possible to observe, the first melting of ice was around the eutectic temperature of the H_2O-NaCl system (−20.8 °C; Potter and Brown, 1977). The melting temperature of ice (Tmice) ranges from −5.1 to −0.2 °C, and the total homogenization temperatures (Th) range from 257 to 398 °C to the liquid state.

The Raman analyses (Table 4) show very variable proportions of the volatile phases, CO_2 (0 to 61 mol%), CH_4 (25 to 100 mol%) and N_2 (0 to 36.9 mol%). The calculated bulk composition indicates that an aqueous-rich fluid (up to 95 mol%) of low salinity (0.4 to 4.9% $NaCl_{eq.}$) with a density varying from 0.6 to 0.7 g/cm^3 was trapped in this FI type.

6.1.2. Type-II or VLcm-w

These FIs were found only in the interstitial quartz from the prograde skarn (Fig. 9, Table 3). They are polyhedral or ellipsoidal in shape, and their sizes vary between 8 and 25 μm. The inclusions may occur isolated or in small clusters within the quartz crystals, associated with the Type-I inclusions, or along intragranular planes. In the latter case the inclusions were interpreted as pseudosecondary (Roedder, 1984). They show two phases at room temperature with the volumetric fraction of the aqueous phase (flw) between 0.25 and 0.55. Occasionally they have a small and highly birefringent trapped solid, which may be a carbonate. The melting of CO_2 ($TmCO_2$ = −69 to −57.8 °C, Table 4) was always under the triple point of pure CO_2 (−56.6 °C), suggesting the presence of other volatile phases. During heating experiments, some of the inclusions decrepited above 298 °C. The total homogenization (Th) was to the liquid or the vapor state in the range of 300 to 415 °C (Table 4).

The calculated bulk composition also shows that a low saline aqueous-rich fluid of moderate density (Table 4) was trapped in this FI type. According to the microthermometric observation, Raman analyses show that CO_2 is the main component of the volatile phase, ranging between 70 and 87 mol%. Methane (11.4 to 28.6 mol%) and N_2 (1.1 to 2.2 mol%) are in lesser proportions (Table 4).

6.1.3. Type-III or VLc-w

These FIs were found only in quartz (Qz2) from veins of the second retrograde stage in association with the pyrite and arsenopyrite (Apy2) deposition (Table 3). They are polyhedral, ellipsoidal or irregular in shape, and their sizes vary between 9 and 27 μm. The inclusions may occur isolated or in small clusters within the quartz crystals and were interpreted as primary (Roedder, 1984). These FI may show two or three phases at room temperature. The volumetric fraction of the aqueous phase (flw) was between 0.05 and 0.50, with a mode from 0.05 to 0.1. The melting of CO_2 ($TmCO_2$ = −57.5 to −56.9 °C, Table 4) indicates that it is the main volatile phase. The $ThCO_2$ was between 23 and 26.9 °C (Table 4) to the liquid or the vapor state. The Th (300 to 325 °C, Table 4) was also to the liquid or the vapor state.

Raman analysis carried out in two inclusions shows small quantities of CH_4 (2.1 to 3 mol%) and N_2 (0.7 to 1.3 mol%) (Table 4). Nevertheless, the bulk composition of the fluid trapped in this FI type was calculated taking into account a volatile phase constituted by 100% CO_2 (Table 4). The H_2O/CO_2 ratio of the fluid trapped is highly variable (between 0.17 and 6.8) whereas the salinity is low (3.2 to 5% $NaCl_{eq}$) and similar to the fluids trapped in the previous FI types.

6.1.4. Type-IV or Lw, Lw-s

These FIs were found in almost all the studied samples (Fig. 10). They occur aligned in transgranular healed microfissures, so they are considered secondary and later with respect to the other FI types. These FIs are especially common in quartz crystals (Qz2) from veins related to the second stage of retrograde alteration. On some occasions, the FIs coexist with small blebs (<20 μm) of opaque minerals (mainly native-Bi and hedleyite) in the same healed fractures (Fig. 10). The FIs accompany or wet the blebs suggesting that they formed at the same time. The inclusions are polyhedral, ellipsoidal or irregular in shape, and their sizes vary between 8 and 36 μm. These FIs show two phases at room temperature, the volumetric fraction of the aqueous phase (flw) lying between 0.6 and 0.95. As previously commented, some

Please cite this article as: Martínez-Abad, I., et al., The Vilalba gold district, a new discovery in the Variscan terranes of the NW of Spain: A geologic, fluid inclusion and stable isotope study, Ore Geol. Rev. (2014), http://dx.doi.org/10.1016/j.oregeorev.2014.10.021

Table 4
Microthermometric and Raman data, and estimated bulk composition of the selected fluid inclusions from each type defined in the Vilalba gold district.

Localization	Type	Microthermometric data						Raman data			Bulk composition					
		$TmCO_2$	$TmCH_4$	Tm ice	Tm Cl	Th CO_2	Th (°C)	CO_2	CH_4	N_2	H_2O	CO_2	CH_4	N_2	D (g/cm^3)	Sal. (% $NaCl_{eq.}$)
Castro de Rei	Type-I Lw-(cm)	–	–	(−5.1, −0.2) −0.9 *39*	(5.9, 17.5) 11.5 *37*	–	(257, 398) L 350 *41*	(0, 61) *10*	(25, 100) *10*	(0, 36.9) *10*	(89, 95.3) *10*	(0, 5.7) *10*	(0.6, 11.8) *10*	(0, 3) *10*	(0.6, 0.7) *10*	(0.4, 4.9) *10*
	Type-II VLcm-w	(−69, −57.8) −59.6 *16*	–	(−7.4, −0.5) −3.5 *15*	(10.5, 13.1) 10.5 *16*	(−4.8, 9.3) L,V −4.5 *15*	(300, 415) V,L 343[a] *11*	(69.8, 87.5) *5*	(11.4, 28.6) *5*	(1.1, 2.2) *5*	(89.5, 92) *5*	(5.9, 7) *5*	(0.5, 1.8) *5*	(0, 0.1) *5*	(0.56, 0.65) *5*	(2.9, 3.7) *5*
	Type-III VLc-w	(−57.5, −56.9) −56.9 *18*	–	(−5.3, −2.8) −2.9 *10*	(8.7, 10.4) 9.7 *19*	(23, 26.9) L,V 26.5 *17*	(300, 325) V,L 310 *13*	(96.6, 100) *5*	(2.1, 3) *5*	(0.7, 1.3) *5*	(14.4, 84.9) *5*	(12.4, 85.1) *5*	–	–	(0.63, 0.82) *5*	(3.2, 5) *5*
	Type-IV Lw/Lw-s	–	–	(−4.1, −0.1) −0.1 *78*	–	–	(105, 296) L 195 *115*	–	–	–	(95.8, 99.9) *20*	–	–	–	(0.81, 0.89) *20*	(0.2, 6.6) *20*
Valiña–Azúmara	VLcm-w1	(−78, −61.6) −61.6 *12*	–	(−4.2, −1) −2.2 *13*	(13.4, 18) 14.8 *14*	(−18.5, 7.5) L −3.6 *9*	(300, 350) V,L 327[a] *4*	(73.2, 85) *6*	(14.3, 25.7) *6*	(0.8, 1.8) *6*	(26, 41.7) *6*	(40.8, 62.1) *6*	(10, 16.4) *6*	(0.6, 1) *6*	(0.57, 0.7) *6*	(6, 8.7) *6*
	VLcm-w2	–	(−87.8 −82.2)V −84,4[a] *5*	(−2.8, −1) −1.5 *5*	(15.5, 19.2) 17.8 *5*	–	n. d. or dec.	(7, 20) *2*	(78.2, 91) *2*	(1.8, 2) *2*	(65.6, 68.3) *2*	(2.4, 5.9) *2*	(21, 28.7) *2*	(0.6) *2*	(0.44, 0.57) *2*	0 *2*
	Lw	–	–	(−3.3, −0.8) −1 *8*	–	–	(140, 226) L 215 *13*	–	–	–	(97, 99) *8*	–	–	–	(0.88, 0.9) *8*	(1.4, 5.4) *8*
Arcos	Lw-(cm)	–	–	(−5.1, −0.8) −2.4 *15*	(10.5–13.7) 10.8 *12*	–	(260–350) L 285 *17*	(42, 91.4) *6*	(8.6, 58) *6*	–	(91.8, 94.4) *6*	(2.9, 4.6) *6*	(0.2, 2.1) *6*	–	(0.74, 0.8) *6*	(1.1, 4.7) *6*
	Lw-(c)	–	–	(−6.6, −1.7) −3.6 *38*	(4.8–9.1) 7.8 *35*	–	(154–273) L 213 *39*	100 *5*	–	–	(92.8, 94.4) *5*	(3.7, 4.4) *5*	–	–	(0.73, 0.8) *5*	(2.8, 5.5) *5*
	Lw—c	(−57,5, −56,6) −56,9 *52*	–	(−4.1, −0.1) −3.4 *63(Fl) 5(Sp)*	(7.9–10) 9.9 *71(Fl) 5(Sp)*	(25.6–30.5)L,V 29.1 *68(Fl) 3(Sp)*	(186–261) L 223 *33(Fl) 3(Sp)*	100 *8*	–	–	(80.6, 89.4) *8*	(7.5, 17.8) *8*	–	–	(0.71, 0.9) *8*	(3, 5.7) *8*
	Lw	–	–	(−3.4, −1.4) −1.5 *8*	–	–	(150 a 267)L 212 18	–	–	–	(97.4, 98.5) *8*	–	–	–	(0.84, 0.9) *8*	(2.4, 2.9) *8*

Compositions are given in mol%; $TmCO_2$: melting temperature of CO_2; $ThCO_2$: homogenization temperature of CO_2; TmCl: melting temperature of clathrate; Tmice: melting temperature of ice; Th: total homogenization temperatures; L: liquid state; and V: vapor state. All temperatures in °C. Range (first line), mode (second line) and number of measurements (third line, italics) are given for each type of fluid in each occurrence. Nv: not visible; dec: decrepited inclusions; *Fl*: fluorite; *Sp*: sphalerite.

[a] Type I was not analyzed by Raman (see text for more details).

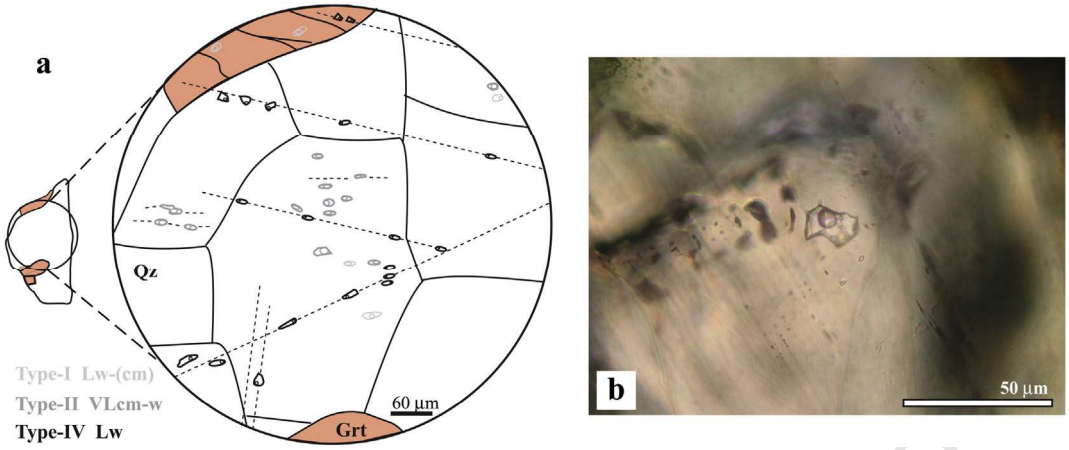

Fig. 9. a) Schematic distribution of fluid inclusions in a sample of the Castro de Rei skarn b) Photomicrograph of a Type-I fluid inclusion in a garnet crystal (PPL).

inclusions show opaque solids that may occupy up to 90% of the total volume of the inclusion (Fig. 10). The first melting of ice was around the eutectic temperature of the H_2O–NaCl system (−20.8 °C; Potter and Brown, 1977), and the Tmice was between −4.1 and −0.1. The Th took place in the range of 105 to 296 °C (Table 4) to the liquid state, the most frequent interval lying between 180 and 220 °C. On heating, the opaque blebs wetted by the fluid inclusions were totally molten, changing progressively from a polyhedral or irregular shape to a final rounded one. The final melting temperature was characterized by the sudden displacement of the bleb within the inclusion at 271 to 272 °C. These temperatures suggest that the blebs were mainly formed by native-Bi (native-Bi melting point = 271.4 °C, Okamoto and Tanner, 1990).

The fluid trapped in this FI type is of very low salinity (0.2 to 6.6% $NaCl_{eq}$) and shows a density ranging from 0.81 to 0.89 g/cm^3 (Table 4).

6.2. Fluid inclusions from Valiña–Azúmara

The fluid inclusions study in Valiña–Azúmara was performed in quartz crystals from a vein hosted by calcareous and black slates. The vein comprises quartz, calcite, arsenopyrite and pyrite from the first stage of mineralization (Au–As). Moreover, sphalerite, sulfosalts and chlorite from the second stage of mineralization (Ag–Pb–Zn–Cu–Sb) occur infilling microveins and interstitial cavities.

Three different types of fluid inclusion were defined: two types aqueous-carbonic (VLcm-w1 and VLcm-w2) and the other one aqueous (Lw) (Table 3). These types are described below and microthermometric results and Raman analyses of the volatile phase are summarized in Table 4.

6.2.1. Type VLcm-w1

These FIs are polyhedral or ellipsoidal in shape, their sizes varying between 12 and 24 µm. They are randomly distributed within the quartz crystals, isolated or in small clusters, being interpreted as primary (Roedder, 1984). They show two phases at room temperature with the volumetric fraction of the aqueous phase (flw) lying between 0.1 and 0.35. The melting of CO_2 ($TmCO_2$ = −78 to −61.6 °C, Table 4) was also below the melting point of pure CO_2 (−56.6 °C), suggesting the presence of other volatile phases. The $ThCO_2$ was between −18.5 and 7.5 °C (Table 4), always to the liquid state. Most of the inclusions homogenized (Th from 300 to 350 °C, Table 4) to the vapor state, while only a few inclusions homogenized to the liquid one. However, most of them decrepited at temperatures above 254 °C.

According to the Raman analyses (Table 4), the volatile phase is mainly constituted by CO_2 (73 to 85 mol%), with variable amounts of CH_4 (14 to 25 mol%) and N_2 (≤1.8 mol%). The calculated bulk composition indicates that a CO_2-rich fluid (40 to 62 mol%) of moderate salinity (6 to 8.7% $NaCl_{eq.}$) and density varying from 0.57 to 0.7 g/cm^3 was trapped in this FI type.

6.2.2. Type VLcm-w2

These FIs are scarce and occur within the quartz crystals associated with the previous FI type. They have been differentiated due to their behavior during the microthermometric studies. During freezing, the bubble became two-phase, indicating that the volatile is mainly CH_4. The volumetric ratio between CH_4 vapor and liquid phases ranges from 60 to 75%. On warming, the two methane phases homogenized (Th CH_4) at temperatures between −87.8 and −82.2 °C, to the vapor phase. These temperatures are close to or below the pure CH_4 critical

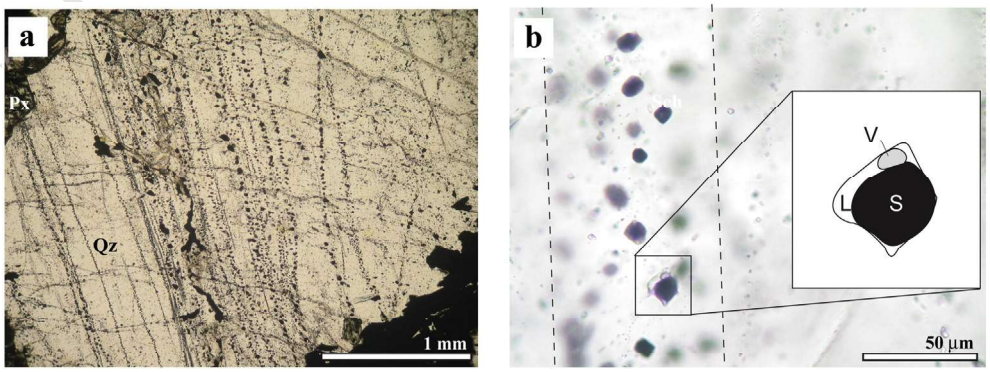

Fig. 10. a) Trails of blebs crossing quartz (Qz) grains of the prograde skarn of Castro de Rei. b) Lw-s type inclusions in the same healed fracture with ore blebs (black). In the box on the right there is a magnification of a Lw-type fluid inclusion that is wetting the bleb (S). Px: Pyroxene.

Please cite this article as: Martínez-Abad, I., et al., The Vilalba gold district, a new discovery in the Variscan terranes of the NW of Spain: A geologic, fluid inclusion and stable isotope study, Ore Geol. Rev. (2014), http://dx.doi.org/10.1016/j.oregeorev.2014.10.021

point (−82.1 °C, Burrus, 1981), indicating the presence of other volatiles. The Raman analyses indicate small amounts of CO_2 (up to 20 mol%) and N_2 (up to 2 mol%) (Table 4). All the FIs decrepited in the temperature range of 294 to 324 °C, before the total homogenization. The calculated bulk composition indicates that a volatile-poor fluid (up to 68 mol% of H_2O) of low salinity and density varying from 0.44 to 0.57 g/cm^3 was trapped in this FI type.

6.2.3. Type Lw

These FIs are irregular in shape, their size varying between 12 and 20 μm. They often occur aligned in transgranular healed microfissures, so they are considered secondary and later with respect to the other FI types. These FIs are associated with sulfosalts from the second mineralization stage. They show two phases at room temperature, the volumetric fraction of the aqueous phase (flw) lying between 0.6 and 0.85. The first melting of ice was around the eutectic temperature of the H_2O-NaCl system (−20.8 °C; Potter and Brown, 1977). The final melting of ice (Tmice) was between −0.8 and −3.3, whereas the Th was between 140 and 226 °C (Table 4) to the liquid state.

The calculated bulk composition indicates that a low-saline aqueous fluid (1.4 to 5.4% $NaCl_{eq}$) with a density ranging from 0.88 to 0.9 g/cm^3 (Table 4) was trapped in this FI type.

6.3. Fluid inclusions from Arcos

The fluid inclusion study was performed in quartz crystals from both a vein and a jasperoid related to the first stage of mineralization (As-Au), and also in fluorite and sphalerite crystals from 2 veins related to the second stage of mineralization (Ag–Pb–Zn–Cu–Sb) (Table 3). Four types of fluid inclusion were defined. Three of them are aqueous-carbonic Lw-(cm), Lw-(c) and Lw-c, and the other one is aqueous (Lw) (Table 3). These types are described below and microthermometric results and Raman analyses of the volatile phase are summarized in Table 4.

6.3.1. Type Lw-(cm)

These FIs were found in quartz crystals related to the arsenopyrite and pyrite mineralization (Table 3). They are polyhedral or irregular in shape, their sizes varying between 4 and 12 μm. They occur isolated or in small clusters and are interpreted as primary (Roedder, 1984). The inclusions show two phases at room temperature with the volumetric fraction of the aqueous phase (flw) between 0.5 and 0.75. The presence of a volatile component was only detected as a result of clathrate formation. The melting temperature of clathrate (Tm Cl) was from 10.5 to 13.7 °C, suggesting the presence of other volatiles apart from CO_2. Only on few occasions was it possible to observe the first melting of ice, occurring close to the eutectic temperature of the H_2O–NaCl system (−20.8 °C; Potter and Brown, 1977). The melting temperature of ice (Tmice) ranges from −5.1 to −0.8 °C, and the total homogenization temperatures (Th) range from 260 to 350 °C to the liquid state.

Raman analyses (Table 4) of the volatile phase indicate the absence of N_2, and variable amounts of CO_2 (42 to 91.4 mol%) and CH_4 (8.6 to 58 mol%). The calculated bulk composition indicates that a volatile-poor fluid (up to 94.4 mol% of H_2O) of low salinity (1.1 to 4.7% $NaCl_{eq.}$) and density varying from 0.74 to 0.8 g/cm^3 was trapped in this FI type.

6.3.2. Type Lw-(c)

These FIs were found in quartz crystals from the jasperoid sample. They are polyhedral or irregular in shape and their sizes vary between 4 and 20 μm. They often occur isolated within the quartz crystals, and are thus interpreted as primary (Roedder, 1984). The inclusions show two phases at room temperature with the volumetric fraction of the aqueous phase (flw) between 0.55 and 0.8. The volatile component was also only detected through clathrate formation. In this case the Tm Cl took place below 10 °C (Table 4), indicating that CO_2 is the main volatile. The total homogenization temperatures (Th) range from 154 to 273 °C to the liquid state, with a mode around 213 °C.

On the basis of microthermometric results, CO_2 was considered to be the only volatile phase of the fluid. The calculated bulk composition indicates that a volatile-poor fluid (up to 94.4 mol% of H_2O) of low salinity (2.8 to 5.5% $NaCl_{eq.}$) and density varying from 0.73 and 0.8 g/cm^3 was trapped in this FI type.

6.3.3. Type Lw-c

These FIs were found in fluorite and sphalerite crystals from two veins related to the second stage of mineralization (Table 3). They are polyhedral or ellipsoidal in shape. Their sizes vary between 8 and 16 μm in the sphalerite crystals and between 30 and 60 μm in the fluorite crystals. In both cases the inclusions often occur isolated or in small clusters, although in the fluorite crystals some inclusions also occur aligned in healed intragranular microcracks. These inclusions are interpreted as being primary and pseudosecondary (Roedder, 1984). They show three phases at room temperature, with the volumetric fraction of the aqueous phase (flw) between 0.4 and 0.8. In fluorite crystals, some FIs show a small trapped solid of elevated birefringence that may be a carbonate. The melting of CO_2 ($TmCO_2$ = −56.6 to −57.5 °C, Table 4) is close to the melting point of pure CO_2 (−56.6 °C), suggesting that it is the main component of the volatile phase. The $ThCO_2$ was between 25.6 and 30.5 °C (Table 4) to the liquid or the vapor state in the case of the fluorite crystals, and always to the liquid state in the case of the sphalerite crystals. The Th always took place to the liquid state, at temperatures ranging from 186 to 261 °C (Table 4), the most frequent values lying between 206 and 245 °C.

The bulk composition of the fluid trapped in this FI type was calculated, assuming CO_2 to be the only volatile phase of the fluid. The fluid trapped is aqueous-carbonic with a low volatile content (7.5 to 17.8 mol% of CO_2). Furthermore, it is of low salinity (3 to 5.7% $NaCl_{eq.}$), and shows a density varying from 0.7 to 0.9 g/cm^3.

6.3.4. Type Lw

These inclusions were found in quartz crystals from the same sample as the Lw-(cm) type. The Lw-type inclusions occur as transgranular trails. They are considered secondary and later with respect to the Lw-(cm) type. The Lw-type inclusions are mainly irregular in shape, and their sizes vary between 12 and 20 μm. These FIs show two phases at room temperature, the volumetric fraction of the aqueous phase (flw) lying between 0.7 and 0.85. The first melting of ice was around the eutectic temperature of the H_2O–NaCl system (−20.8 °C; Potter and Brown, 1977). The final melting of ice (Tmice) was between −3.4 and −1.4, whereas the Th was between 150 and 267 °C (Table 4) to the liquid state.

The calculated bulk composition indicates that a low-saline aqueous fluid (2.4 to 2.9% $NaCl_{eq}$) with a density ranging from 0.84 to 0.9 g/cm^3 (Table 4) was trapped in this FI type.

7. Stable isotope systematics

The isotopic composition of O in silicates, O and C in carbonates and S in sulfides was measured in order to determine the origin of the hydrothermal fluids involved in the mineralization of the Vilalba gold district.

7.1. Oxygen in silicates

The O isotope composition was measured in 12 samples of garnet, pyroxene and quartz from the Castro de Rei skarn, 3 quartz samples of hydrothermal veins from Valiña–Azúmara, and 7 quartz samples of jasperoids and hydrothermal veins from Arcos. The results are compiled in Table 5.

In Castro de Rei, 9 of the analyzed samples were from the garnet–pyroxene–quartz and pyroxene–quartz prograde skarns. Garnet and

Please cite this article as: Martínez-Abad, I., et al., The Vilalba gold district, a new discovery in the Variscan terranes of the NW of Spain: A geologic, fluid inclusion and stable isotope study, Ore Geol. Rev. (2014), http://dx.doi.org/10.1016/j.oregeorev.2014.10.021

Table 5
Oxygen and carbon isotope analyses of silicates and carbonates from the mineralizations of the Vilalba gold district. The $\delta^{18}O_{fluid}$ data calculated from Bottinga and Javoy (1973, 1975) and Zheng (1993, 1999).

Location	Sample	Mineral	$\delta^{18}O_{SMOW}$	$\delta^{13}C_{PDB}$	T[a] (°C)	$\delta^{18}O_{fluid}$	$\Delta\delta^{18}O$
Castro de Rei (CDR)							
Marble	7-409	Cal	12.1	−3.1			
	7-377	Cal	12.7	−0.7			
	7-409b	Cal	11.7	−2.9			
Prograde Grt–Px skarn (proximal skarn)	2 T	Grt	8.3		520 a 560	9.5/9.7	534 °C
	2 T	Qz	12.3			9.5/9.9	(Qz-Grt)
	14-390	Qz	12.2			9.4/9.8	
	4 M	Grt	7.7			8.9/9.1	
	4 M	Px	8.1			9.5/9.7	
	11-330	Grt	7.9			9.1/9.5	
	17-647a	Cal	10.8	−11.3		8.6/8.9	
	11-330	Cal	9.8	−10.0		7.5/7.9	
Prograde Px skarn (distal skarn)	11-326	Qz	11.9		520 a 560	9.1/9.4	
	11-326	Px	9.1			10.5/10.7	
	11-334	Px	8.8			10.2/10.4	
	7-409c	Cal	12.7	−8.2		10.5/10.8	
	7-447	Cal	11.2	−8.7		9.0/9.3	
	7-447b	Cal	11.0	−8.6		8.8/9.1	
	11-331	Cal	11.0	−12.4		8.8/9.1	
	11-333	Cal	10.4	−11.7		8.2/8.5	
	11-333b	Cal	9.7	−11.2		7.5/7.8	
	12–528	Cal	11.3	−11.9		9.1/9.4	
1st retroskarn stage	4Q	Cal1	10.6	−9.0	370 a 518	6.4/8.3	
2nd retroskarn stage	7-350	Qz2	13.7		354 a 388	8.2/8.9	
	7-144	Qz2	14.3			8.8/9.5	
	17-37	Qz2	13.8			8.3/9.0	
	6-408	Cal3	9.0	−6.8	285 a 315	2.8/3.6	
Valiña–Azúmara (VA)							
Hydrothermal veins	4-40	Qz	13.9		355 a 450	8.4/10.3	
	Sab1	Qz	14.4			8.9/10.8	
	4-61	Qz	14.8			9.2/11.2	
Arcos (Ar)							
Jasperoids	Jarcv	Qz	14.1		312 a 383	7.2/9.1	
	Jarc	Qz	12.5			5.6/7.5	
	3-17	Qz	12			5.0/7.0	
	3-57	Qz	15.2			8.3/10.2	
	20,89	Qz	15.4			8.5/10.4	
Hydrothermal veins	2-88	Qz	15.1		312 a 383	8.2/10.1	
	24-31	Qz	16.2			9.3/11.2	

pyroxene show similar $\delta^{18}O_{SMOW}$ values, from 7.7 to 9.1‰, whereas the quartz samples show $\delta^{18}O_{SMOW}$ values ranging from 11.9 to 12.3‰. Isotopic fractionation between quartz and garnet ($\Delta^{18}O = 4‰$) yields a temperature of 534 °C (Table 5), which is in accordance with the range of temperatures from 520 to 560 °C estimated for the contact metamorphism in this area. The rest of the analyzed samples are quartz (Qz2) from veins related to the second retrograde stage, in association with the pyrite and arsenopyrite deposition. The isotopic composition of these samples varies between 13.7 and 14.3‰ $\delta^{18}O_{SMOW}$.

In Valiña–Azúmara, the 3 analyzed samples were quartz veins related to the first stage of mineralization (Au–As), in association with the pyrite and arsenopyrite deposition. The $\delta^{18}O_{SMOW}$ values obtained range from 13.9 to 14.8‰. In Arcos, 5 of the analyzed samples are of quartz from jasperoid rocks, and their isotopic compositions range from 12 to 15.4‰ $\delta^{18}O_{SMOW}$. The other 2 samples are of quartz from hydrothermal veins, which are also associated with the pyrite and arsenopyrite deposition. The isotopic compositions of these samples vary between 15.1 and 16.2‰ $\delta^{18}O_{SMOW}$ (Table 5).

7.2. Carbon and oxygen in carbonates

The C and O isotope composition was measured in a total of 14 samples of carbonates from the Castro de Rei skarn: 3 samples from marble, 9 samples from skarn calcites (Cal), interstitial to garnet, pyroxene and quartz crystals, and 2 samples of calcite related to the retroskarn alteration [one associated with epidote and amphibole (Cal1) and the other associated with chlorite (Cal3)]. The results are compiled in Table 5 and Fig. 11.

The marble samples show isotopic compositions ranging from −3.1 to −0.7‰ of $\delta^{13}C_{PDB}$, and from 11.7 to 12.7‰ of $\delta^{18}O_{SMOW}$. The skarn calcites show values of $\delta^{13}C_{PDB}$ between −12.4 and −8.2‰, and values

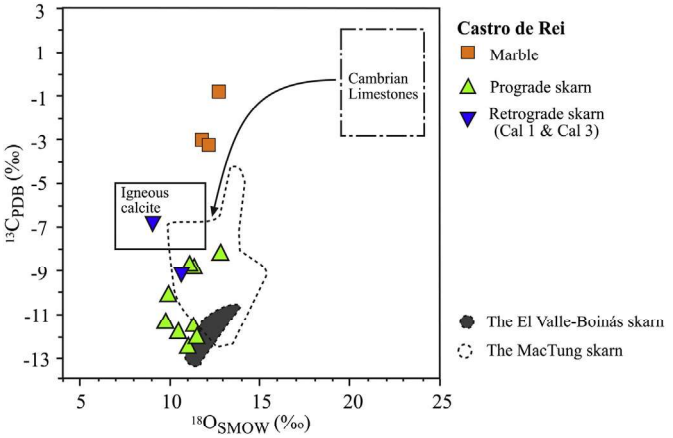

Fig. 11. Plot of the $\delta^{13}C_{PDB}$ and $\delta^{18}O_{SMOW}$ values of the analyzed carbonates in the Vilalba gold district. In the diagram, calcite from other skarn deposits are also included (El Valle-Boinás, Cepedal et al., 2000; MacTung, Gerstner et al., 1989). Values of Cambrian limestones after Veizer and Hoefs (1976). Values for calcite in carbonaceous shale from Hofstra and Cline (2000). Igneous calcite after Bowman (1998).

of $\delta^{18}O_{SMOW}$ between 9.7 and 12.7‰. In the case of the retroskarn-related calcite, the $\delta^{13}C_{PDB}$ and $\delta^{18}O_{SMOW}$ values obtained range from −6.8 to −9‰ and from 9 to 10.6‰, respectively (Table 5).

As observed in Fig. 11, the isotopic compositions of the calcites from the Castro de Rei skarn mineralization are greatly depleted in ^{18}O and ^{13}C relative to unaltered carbonated sediments. The ^{18}O-depleted values of the calcites can be explained by metasomatic processes in the skarn deposits (Bowman et al., 1985) resulting from the interaction between a magmatic hydrothermal fluid depleted in ^{18}O- and ^{13}C and the host limestone. The $\delta^{13}C_{PDB}$ values of the calcites from Castro de Rei are depleted in ^{13}C (up to −12.4‰, Table 5) with respect to the igneous carbon (from −5 to −8‰; Bowman, 1998), suggesting the contribution of ^{13}C-depleted carbon from the organic matter hosted in the metasedimentary rocks. These ^{13}C-depleted values have been documented in other skarns such as Mac Tung (Northwest Territories, Gerstner et al., 1989) and El Valle-Boinás (North of Spain, Cepedal et al., 2000), where methane-rich fluid inclusions were also documented.

7.3. Sulfur

The sulfur isotope composition was measured in 24 samples of different sulfides (pyrrhotite, pyrite, arsenopyrite and sphalerite) from the three mineralized areas: 20 samples from Castro de Rei, 3 samples from Valiña–Azúmara and 1 sample from Arcos. The results are compiled in Table 6.

In the Castro de Rei skarn, the sulfides analyzed are representative of the different stages of sulfide deposition. Pyrrhotite and arsenopyrite (Apy1) samples of the first stage of retrogradation show $\delta^{34}S_{CDT}$ values that range between 2.7 and 5.9‰ (Table 6). For the second stage of retrogradation, 12 arsenopyrite (Apy2) samples and one of sphalerite were analyzed. These sulfides show heavier isotopic compositions than the first ones, ranging between 7.8 and 10.9‰ $\delta^{34}S_{CDT}$ (Table 6). In Valiña–Azúmara, 2 samples of arsenopyrite and 1 of pyrite were analyzed, both sulfides belonging to the first stage of mineralization (Au–As). The $\delta^{34}S_{CDT}$ values obtained, between 7.5 and 8.1‰ (Table 6), are similar to those obtained for the sulfides of the second retrograde stage of the Castro de Rei skarn. The analyzed pyrite from Arcos shows a value of $\delta^{34}S_{CDT} = 11.2$‰, which is slightly heavier than that obtained in Castro de Rei.

8. Discussion and conclusions

8.1. Global fluid composition

The volatile and bulk composition of the trapped fluid from the different types of fluid inclusions described in the foregoing were plotted in CO_2–CH_4–N_2 and H_2O–CO_2–10x(CH_4-N_2) ternary diagrams, respectively (Fig. 12).

In Castro de Rei, the volatile phase of the fluids shows a tendency towards the CO_2 enrichment from Type I to Type III inclusions, whereas the methane and nitrogen concentrations decrease (Fig. 12a). The presence of CH_4 in these fluids is explained by the organic matter content of the Limestone and Slate Fm. In the case of N_2, according to Bebout et al. (1999), a release of nitrogen is produced by the breakdown of NH_4-bearing mica during the prograde metamorphic reactions. Similar N_2- and CH_4-bearing fluids had already been observed in other skarn deposits from the Río Narcea Gold Belt: the El Valle-Boinás Cu–Au skarn and the Ortosa Au skarn (Cepedal, 2001; Cepedal et al., 2003). The highly variable amounts of CH_4 and N_2 in the trapped fluid in the Type-I and the coexistence of these fluid inclusions with the CO_2-richer Type-II fluid inclusions suggest a mixing of two different fluids. Moreover, a CH_4-rich volatile phase infers reduced conditions during the skarn formation that conditioned mineral assemblages. The trend of enrichment in CO_2 of the fluids suggests an evolution towards higher fO_2 conditions during the second retrograde stage, when the carbonatization of the host-rocks and alteration of the pyrrhotite to pyrite and marcasite took place. Considering the calculated bulk composition from Type I to Type IV inclusions (Fig. 12b), we concluded that the trapped hydrothermal fluid evolved to a more water-rich fluid by loss of volatiles with relatively constant salinity.

The volatile composition of the trapped fluids in Valiña–Azúmara and Arcos is plotted in Fig. 12c. Similar to Castro de Rei, in both areas there are aqueous-carbonic fluids with variable amounts of CH_4, but with very little or no N_2. The presence of CH_4 can also be explained by the organic matter content of the host rocks. In Arcos the mineralization is hosted by impure limestones and calcareous slates, while in Valiña–Azúmara the host rocks are mainly calcareous and black slates. This fact may explain the higher proportions of CH_4 in the trapped fluids of the latter area. Moreover, neither mineralized area was affected by contact metamorphism that could release nitrogen. This fact would

Table 6
Sulfur isotope data for sulfide minerals from the mineralizations of the Vilalba gold district.

Localization	Sample	Mineral	$\delta^{34}S_{(CDT)}$ (‰)	T[a] (°C)	$\delta^{34}S_{H2Sfluid}$ (‰)
Castro de Rei (CDR)	CA-11-334	Po	4.6	370–518 °C	4.4 ± 0.04
First stage of retroskarn (*CDR-1*)	CA-6-458	Po	5.9		5.7 ± 0.04
	CA6-44.75	Po	4.1		3.9 ± 0.04
	CA6-5.35	Apy1	5.3		4.5 ± 0.17
	CA-2-57	Po	3.2		3.0 ± 0.04
	CA2-56.9	Po	2.7		2.5 ± 0.04
	CA2-55.2	Po	3.6		3.4 ± 0.04
Second stage of retroskarn (*CDR-2*)	CA7-350	Apy2	9.2	354–388 °C	8.2 ± 0.05
	CA7-144	Apy2	10.9		9.9 ± 0.05
	CA7-37	Apy2	9.9		8.9 ± 0.05
	CA-6-148	Apy2	8.9		7.9 ± 0.05
	CA5-456	Apy2	8.4		7.4 ± 0.05
	CA5-274	Apy2	8.1		7.1 ± 0.05
	CA5-155.6	Apy2	10.0		9.0 ± 0.05
	CA-5-127	Apy2	10.9		9.9 ± 0.05
	CA-4-109	Apy2	10.2		9.2 ± 0.05
	CA-3-45	Apy2	10.5		9.5 ± 0.05
	CA1-68	Apy2	7.8		6.8 ± 0.05
	CA-1-56	Apy2	8.9		7.9 ± 0.05
	CA17-37	Sph	8.9	285–315 °C	8.6 ± 0.02
Valiña–Azúmara (VA)	VAL-4-40	Py	7.5	355–450 °C	6.6 ± 0.13
	SAB-1	Apy	7.8		6.9 ± 0.13
	SAB-2	Apy	8.1		7.2 ± 0.13
Arcos (AR)	CH-32-54	Py	11.2	312–383 °C	10.2 ± 0.12

Please cite this article as: Martínez-Abad, I., et al., The Vilalba gold district, a new discovery in the Variscan terranes of the NW of Spain: A geologic, fluid inclusion and stable isotope study, Ore Geol. Rev. (2014), http://dx.doi.org/10.1016/j.oregeorev.2014.10.021

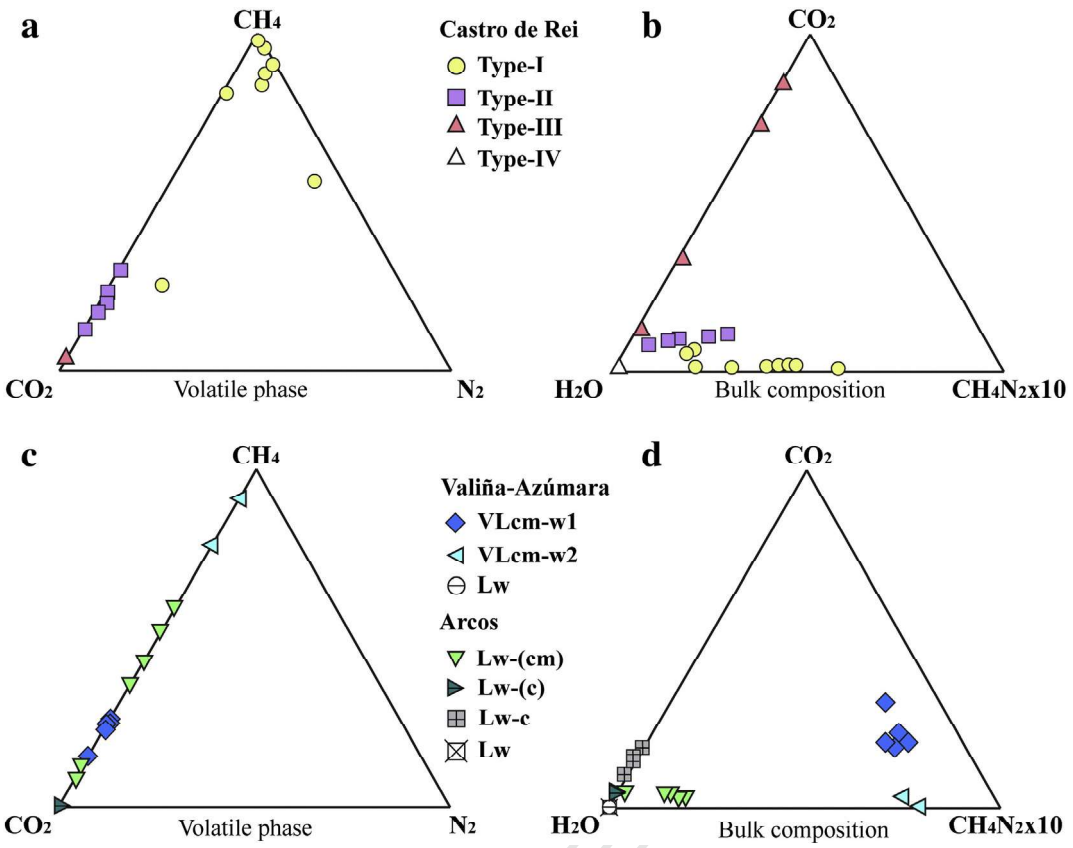

Fig. 12. Compositional ternary plots of the volatile-rich phase and bulk fluid composition of the different fluid inclusions types measured: a), b) Castro de Rei skarn; c), d) Valiña–Azúmara and Arcos.

explain the lower amounts of N_2 in the hydrothermal fluids. In the bulk composition diagram, it is noticeable that the fluids from Arcos are richer in water than the fluids from Valiña–Azúmara and Castro de Rei (Fig. 12d). The evolution observed in the Arcos area is quite similar to that observed in Castro de Rei: the volatile phase tends towards an enrichment in CO_2 and the trapped hydrothermal fluid evolved to an enriched-water fluid. This evolution pattern is not so clear in Valiña–Azúmara since the CO_2 rich fluid has not been found in the samples from this area. However, similar to what is observed in the previous mineralized areas, the last trapped fluid in Valiña–Azúmara related to the second stage of mineralization (Ag–Pb–Zn–Cu–Sb) is also aqueous in composition (type Lw).

8.2. P–T reconstruction (ore-forming conditions)

A reconstruction of the pressure–temperature conditions of formation of the three mineralized areas has been carried out on the basis of fluid inclusion isochores (Fig. 13). Isochores were calculated with the ISOC computer program of the FLUIDS package (Bakker, 2003; Bakker and Brown, 2003).

In the Castro de Rei skarn (Fig. 13a), the P–T conditions of the prograde skarn were constrained, taking into account the isochores of the Type I and Type II fluid inclusions and the estimated temperatures for the aforementioned contact metamorphism (520–560 °C). The highest pressure values obtained for Type I isochores are between 2.3 and 2.5 kbar. This interval probably represents a lithostatic pressure, and assuming an average density for the rock column of 2.6 g/cm^3, such pressures indicate a relatively deep structural level of around 9.5 km at the moment of the skarn formation. The pressure values obtained for Type II isochores are slightly lower, ranging from 1.7 to 2 kbar. As previously commented, both types of inclusion coexist in the quartz crystals that are interstitial to the garnet. These lower pressure values suggest a combination of lithostatic pressure and hydrostatic pressure.

As previously mentioned, we could not study FIs related to the first stage of retroskarn. In the case of the second retrograde stage, the two different phases defined are represented by the trapped fluids in Type III and Type IV fluid inclusions. In order to constrain the real trapping P–T conditions, the Type III isochores were combined with the temperature, which ranged from 354 to 388 °C and was obtained with the arsenopyrite geothermometer (Kretschmar and Scott, 1976; Sharp et al., 1985). This temperature range was obtained considering only the data from the core of Apy2 crystals (30.8–31.5 at.% As) since the higher As values obtained in the rims (>33 at.% As) are outside the pyrite–arsenopyrite stability field, suggesting metastable conditions of formation. The pressure interval obtained is between 1.3 and 2.1 kbar, similar to that obtained for the Type II isochores (Fig. 13a). The second phase was characterized by the presence of chlorite and the Au–Bi–Te–S mineralization. Taking into account microprobe analysis of chlorite (Table 7), a quite similar temperature range of between 285 and 315 °C was obtained using different chlorite geothermometers (Cathelineau, 1988; Kranidiotis and MacLean, 1987 and Xie et al., 1997). The intersection between these temperatures and the Type IV isochores results in a range of pressures similar to those obtained for the other inclusion types. In addition, these Type-IV inclusions often present opaque trapped solids, mainly formed by native-Bi (Fig. 10). As previously commented, during heating these opaque solids were totally molten at temperatures between 271 and 272 °C. This fact suggests that they were trapped as blebs of a Bi-rich melt that coexisted with the hydrothermal fluid at that moment. We propose the liquid bismuth collector model (Douglas et al., 2000; Tooth et al., 2008, 2011) as one of the possible mechanisms of gold deposition at the Castro de Rei skarn, which may also explain the close association observed between Au and Bi. The strong partition of gold (up to 20 wt.% Au) into liquid

Please cite this article as: Martínez-Abad, I., et al., The Vilalba gold district, a new discovery in the Variscan terranes of the NW of Spain: A geologic, fluid inclusion and stable isotope study, Ore Geol. Rev. (2014), http://dx.doi.org/10.1016/j.oregeorev.2014.10.021

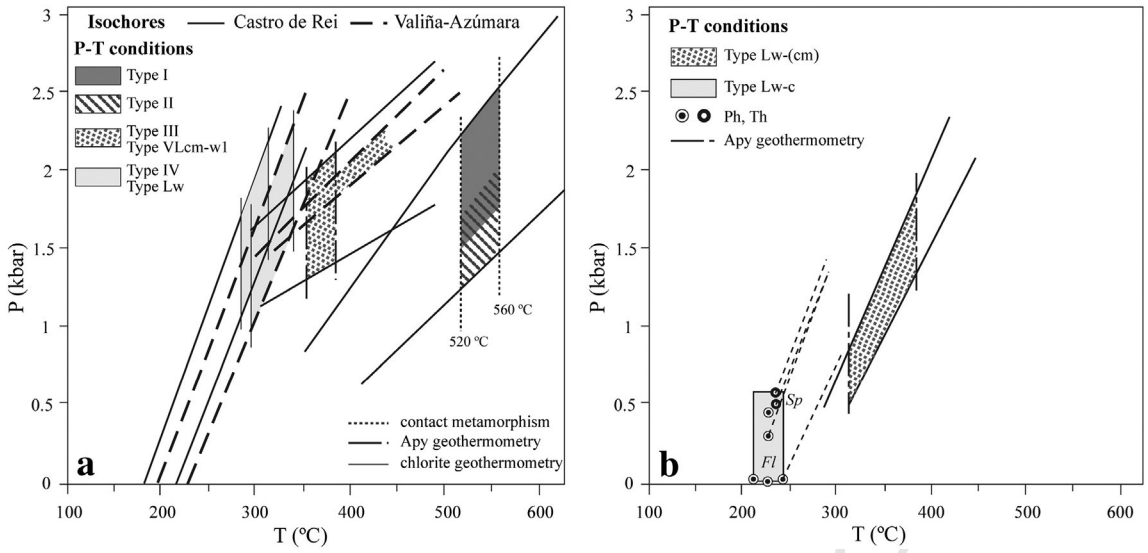

Fig. 13. P–T reconstruction diagram with the representative isochores of the different fluid inclusion types identified in the Vilalba gold district. The circles are the minimum P–T conditions (Ph–Th) for the stage of trapping. The gray and pattern areas indicate the temperature ranges obtained from geothermometry (more details in text): a) data from the Castro de Rei and Valiña–Azúmara areas; b) data from the Arcos deposit.

bismuth from the coexisting hydrothermal fluid (Douglas et al., 2000) can produce the deposition of gold, even when the fluid is significantly gold undersaturated (Tooth et al., 2008).

The estimated P–T conditions for the mineralized area of Valiña–Azúmara are also shown in Fig. 13a. For the first stage of mineralization (Au–As) we have calculated the isochores of the Type VLcm-w1 fluid inclusion observed in a mineralized quartz vein. In order to constrain the P–T conditions we used the composition of the arsenopyrite associated with this stage. The Apy I in Valiña–Azúmara has a composition ranging between 30.8 and 34.1 at.% of As. This range indicates minimum temperatures of 355 °C, in the arsenopyrite–pyrite stability field (Kretschmar and Scott, 1976; Sharp et al., 1985), and pressures around 1.7 kbar. These conditions overlap those obtained in Castro de Rei (Fig. 13a). However, the highest values of As are plotted outside the arsenopyrite–pyrite stability field, suggesting that the arsenopyrite deposition began with pyrrhotite instead of pyrite. The porous texture observed in the Py-I may be considered as evidence of it being a product of pyrrhotite alteration (Murowchick, 1992). In any case, we assume

Table 7
Representative electron microprobe analyses of chlorites from Castro de Rei and Valiña–Azúmara and comparison of geotermometer results. The ranges of the most frequent values obtained (in bold) have been used to constrain P–T trapping conditions.

Sample analysis	Castro de Rei			Valiña–Azúmara		
	2Y C1b	7-166 2	CA2O 3	SAB1 198	SAB1 210	SAB1 225
SiO_2	27.30	28.00	26.40	26.74	27.04	26.30
TiO_2	0.07	0.04	0.01	0.04	0.03	0.08
Al_2O_3	18.33	19.87	19.47	21.73	21.48	21.59
Fe_2O_3	0.00	0.36	0.32	0.58	0.89	0.62
FeO	22.37	18.19	25.92	17.05	15.95	18.60
MnO	0.00	0.05	0.93	0.41	0.42	0.46
MgO	18.54	20.99	14.54	20.10	20.15	18.57
CaO	0.09	0.06	0.05	0.01	0.06	0.05
Na_2O	0.01	0.02	0.00	0.00	0.01	0.00
K_2O	0.01	0.01	0.01	0.00	0.01	0.02
H_2O	11.45	11.83	11.29	11.73	11.70	11.57
Total	98.20	99.48	99.02	98.40	97.78	97.94
On the basis of 28 O						
Si	5.72	5.66	5.60	5.45	5.52	5.44
Al^{IV}	2.28	2.33	2.39	2.54	2.47	2.55
Al^{VI}	2.25	2.41	2.48	2.69	2.72	2.71
Fe^{3+}	0.00	0.05	0.05	0.09	0.14	0.10
Fe^{2+}	3.92	3.08	4.60	2.91	2.73	3.22
Mn	0.00	0.01	0.17	0.07	0.07	0.08
Mg	5.79	6.33	4.60	6.12	6.14	5.73
Ca	0.02	0.01	0.01	0.00	0.01	0.01
Na	0.01	0.01	0.00	0.00	0.01	0.00
K	0.00	0.00	0.00	0.00	0.01	0.01
OH	16.00	16.00	16.00	16.00	16.00	16.00

	Total of 11 analyses ($T_{min-max}$)	Total of 27 analyses ($T_{min-max}$)
Kranidiodis and MacLean (1987)	268–310 °C	286–320 °C
Cathelineau (1988)	277–325 °C	318–356 °C
Xie et al. (1997)	231–308 °C	293–348 °C
Most frequent temperatures	285–315 °C	295–340 °C

Please cite this article as: Martínez-Abad, I., et al., The Vilalba gold district, a new discovery in the Variscan terranes of the NW of Spain: A geologic, fluid inclusion and stable isotope study, Ore Geol. Rev. (2014), http://dx.doi.org/10.1016/j.oregeorev.2014.10.021

that the upper temperature limit for this stage is open since the highest values of As obtained in this arsenopyrite give unrealistically high temperatures (up to 500 °C). The P–T conditions of the second stage of mineralization (Ag–Pb–Zn–Cu–Sb) were constrained taking into account the isochores of the Type Lw fluid inclusions and the temperatures obtained with the chlorite geothermometers (295 to 340 °C, Kranidiotis and MacLean, 1987; Cathelineau, 1988; Xie et al., 1997; Table 7). These conditions also overlap those obtained in Castro de Rei (Fig. 13a).

The estimated P–T conditions for the mineralized area of Arcos are plotted in Fig. 13b. For the first stage of mineralization (Au–As) we have also combined the isochores of the Type Lw-(cm) fluid inclusions studied in a mineralized quartz vein, with the arsenopyrite composition. In order to use the arsenopyrite geothermometer (Kretschmar and Scott, 1976; Sharp et al., 1985), we only considered the Apy-I with Co values below 1 wt.%, resulting in an interval of between 30.2 and 31.4 at.% As. The derived temperature ranges between 312 and 383 °C and corresponds to pressures varying over a wide range, from 0.5 to 1.8 kbar, due to the steep slope of the isochores (Fig. 13b). This fact suggests that it is not possible to constrain the current P–T conditions for this first stage of mineralization in Arcos. Similarly, we were not able to establish the P–T conditions for the second stage of mineralization (Ag–Pb–Zn–Cu–Sb) due to the lack of a suitable geothermometer. The isochores of the Type Lw-c fluid inclusions measured in crystals of sphalerite and fluorite have been plotted in Fig. 13b. The Th–Ph conditions are also shown in the figure. In the fluid inclusions studied in sphalerite crystals, homogenization temperatures indicate minimum pressures between 0.5 and 0.6 Kbar. In the fluorite crystals, the trapping of the aqueous-carbonic fluid in Type Lw-c inclusions took place at minimum conditions (Th–Ph) of between 210 °C and 237 °C, and at pressures from 0.01 to 0.45 kbar (Fig. 13b). A similar pressure drop was observed in fluorite crystals from the Hg deposit of Escarlati in the Cantabrian Zone (Martin-Izard et al., 2009). According to these authors, this drop in pressure probably represents the transition from lithostatic to hydrostatic conditions due to the increase in fracture connectivity generated by a degassing phenomenon. At this level of knowledge, it is not possible to establish more exactly the P–T conditions of formation of the Arcos deposit. However, the homogenization pressures obtained in Arcos are always lower in comparison with the other two mineralized areas, Castro de Rei and Valiña–Azúmara. So we assume that the Arcos deposit was in a shallower emplacement at the moment of its formation.

8.3. Source of the ore-forming materials and fluids

The calculated oxygen isotopic composition of the fluids ($\delta^{18}O_{fluid}$) related to the mineralization is compiled in Table 5 and shown in Fig. 14. The temperatures used for the calculation are the same as those used for the P–T reconstruction. The fluid in equilibrium with the silicates from the prograde skarn has $\delta^{18}O$ values ranging from 8.9 to 10.8‰, whereas the fluid in equilibrium with the retrograde stage shows a slightly lighter composition, between 8.2 and 9.5‰. The calculated $\delta^{18}O_{fluid}$ values from the calcites of Castro de Rei are between 7.5 and 10.8‰ (Table 5), similar to those obtained for the silicates. The $\delta^{18}O_{fluid}$ values calculated from the retrograde stage calcites (Cal3) in association with chlorite are between 2.8 and 3.6‰ (Table 5, Fig. 14), suggesting the influence of a lighter fluid of meteoric origin.

The calculated $\delta^{18}O$ for the hydrothermal fluid in Valiña–Azúmara varies between 8.4 and 11.2‰, values similar to those calculated for Castro de Rei (Fig. 14). In the case of Arcos, the values of $\delta^{18}O_{fluid}$ calculated from the hydrothermal quartz-veins vary from 8.2 to 11.2‰, thus making them similar to the previous ones. However, the values of $\delta^{18}O_{fluid}$ calculated from jasperoids are lighter, between 5 and 10.4‰ (Fig. 14).

In Fig. 14 the $\delta^{18}O_{fluid}$ values of the main oxygen reservoirs are included. The $\delta^{18}O_{fluid}$ values obtained from the hydrothermal minerals

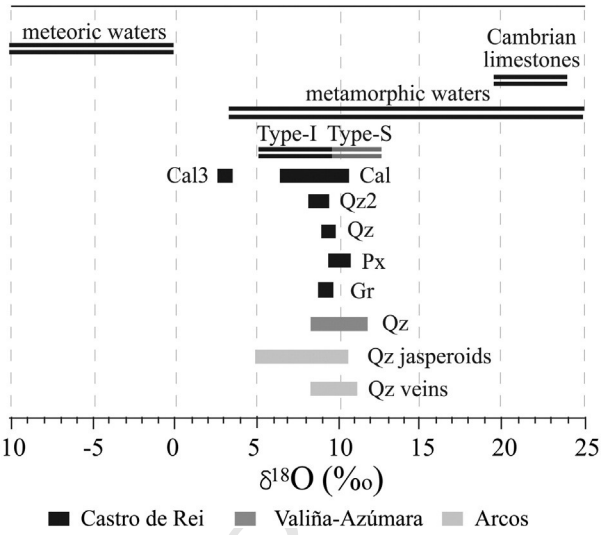

Fig. 14. Plot of the $\delta^{18}O$ values of the fluid in equilibria with the silicates and carbonates of the Vilalba gold district. Values of Cambrian limestones after Veizer and Hoefs (1976). Values for magmatic waters (Type I and S) from Bowman (1998). Values for metamorphic waters from Hofstra and Cline (2000). Values for meteoric waters from Craig (1961).

of the Vilalba gold district overlap the ranges of values for magmatic waters (Bowman, 1998) and metamorphic waters (Hosfstra and Cline, 2000). This fact makes it difficult to establish the origin of the hydrothermal fluids when only taking into account the oxygen isotope composition. Therefore, it will be necessary to consider other factors such as the presence of igneous rocks, the existence of a skarn mineralization as well as the sulfur isotope geochemistry, which will be described below. The lighter $\delta^{18}O_{fluid}$ values obtained, e.g. for the second retrograde stage calcite, and the jasperoids rocks from Arcos suggest the interaction between hydrothermal fluids and meteoric waters, which in the case of Arcos could be explained by the shallower situation of this mineralized area.

The values of $\delta^{34}S_{H2S}$ of the hydrothermal fluid were calculated using the mineral-H_2S equations from Ohmoto and Rye (1979). These values and the temperatures used for the calculation are shown in Table 6. Taking into account the presence of pyrrhotite during the first stage of skarn retrograde alteration, we assume that reduced sulfur is equivalent to total sulfur within the ore fluid, e.g. the $\delta^{34}S_{fluid}$ was between 2.4 and 5.7 (±0.04‰) (Table 6). The sulfur isotopic composition of hydrothermal sulfides is essentially controlled by 1) the isotopic composition of the fluid, 2) the temperature, 3) the amount of sulfide deposited from the fluid, and 4) the fO_2–pH conditions of the fluid (Ohmoto, 1972). Only the initial isotopic composition of the fluid is characteristic of the source, whereas the variations in the other physical–chemical parameters can produce differences in the sulfur isotopic composition of the precipitated sulfides. If we considered an initial value of $\delta^{34}S_{fluid} \approx 3‰$, the precipitation of the heavier sulfides of the second stage would only be possible with a pH increase (Ohmoto, 1972). This pH increase could take place due to the interaction of the hydrothermal fluid with the carbonaceous host rocks. However, values of $\delta^{34}S_{CDT}$ up to 11‰, as obtained for the sulfides of the second stage of retrogradation, would need a high pH increase, which would be difficult to explain. In addition, the destabilization of the early pyrrhotite and the formation of pyrite indicate an evolution towards more oxidized conditions that would produce lighter $\delta^{34}S$ values in the formed sulfides.

The sulfur isotope compositions of the sulfides from Castro de Rei are displayed graphically in Fig. 15, in which the $\delta^{34}S_{CDT}$ values of diagenetic pyrites from slates of the Cabos Fm., Cambrian in age (19 to 22‰, Arias et al., 1997), are included. Also included are $\delta^{34}S_{CDT}$ values of sulfides from several Pb–Zn deposits hosted in Cambrian carbonates (Rubiales, Tornos and Arias, 1993; Antonina and Santa Bárbara, Tornos et al.,

Please cite this article as: Martínez-Abad, I., et al., The Vilalba gold district, a new discovery in the Variscan terranes of the NW of Spain: A geologic, fluid inclusion and stable isotope study, Ore Geol. Rev. (2014), http://dx.doi.org/10.1016/j.oregeorev.2014.10.021

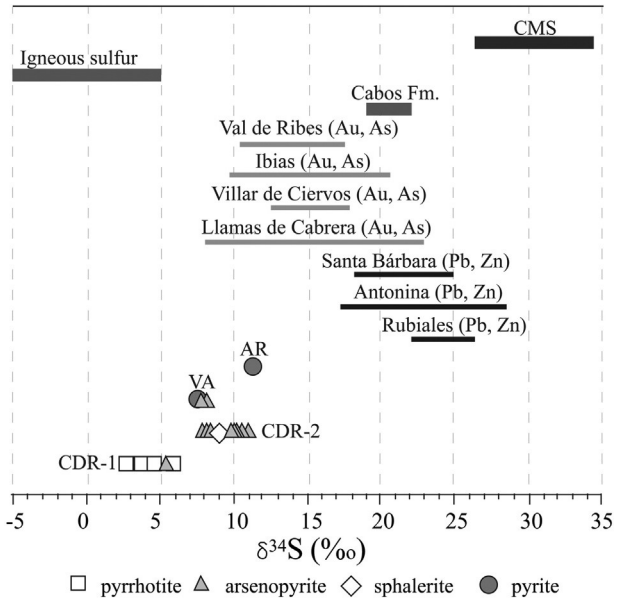

Fig. 15. Plot of the $\delta^{34}S$ values of the analyzed sulfides in the Vilalba gold district. In the diagram, $\delta^{34}S$ range values of sulfides from Pb/Zn deposits (Rubiales, Tornos and Arias, 1993; Antonina and Santa Bárbara, Tornos et al., 1996) located near the district and Au–As deposits (Villar de Ciervos, Ribera et al., 1992; Llamas de Cabrera, Gómez-Fernández et al., 2012; Ibias, Arias et al., 1997; Vall de Ribes, Ayora et al., 1992) from the NW of Spain are also included. $\delta^{34}S$ values from diagenetic pyrites of the Cambrian Cabos Fm. (Arias et al., 1997) as well as the typical $\delta^{34}S$ values from igneous rocks sulfides (Ohmoto and Rye, 1979) and Cambrian marine sulfates (CMS, Claypool et al., 1980) are also included.

1996), all of them located in the vicinity of the Vilalba district. The high $\delta^{34}S_{CDT}$ values of the sulfides from these Pb–Zn deposits (18 to 29‰, Fig. 15) indicate the presence of very heavy sulfur derived by abiogenic reduction of marine sulfates (Tornos et al., 1996).

Other data included in Fig. 15 are the $\delta^{34}S_{CDT}$ values of sulfides from quartz-gold vein deposits hosted by Cambrian–Ordovician rocks: Villar de Ciervos (Ribera et al., 1992); Vall de Ribes (Ayora et al., 1992); Ibias (Arias et al., 1997) and Llamas de Cabrera (Gómez-Fernández et al., 2012). These deposits have been classified as orogenic-gold deposits or mesothermal gold-vein deposits in which the country rocks provided sulfur for the fluid system. The $\delta^{34}S_{CDT}$ values of the sulfides from Valiña–Azúmara and Arcos, in addition to the sulfides from the second stage of retrogradation of Castro de Rei, overlap the lighter values of these quartz–gold vein deposits.

However, the values obtained in the pyrrhotite and arsenopyrite from the first stage of the skarn alteration can only be explained by the occurrence of a hydrothermal fluid with a sulfur isotopic composition as light as ≈3‰ (Table 6). Therefore, a source of sulfur different to the metasedimentary host rocks is necessary. We propose a magmatic source for the sulfur, at least in the earliest episode of the hydrothermal mineralization. Furthermore, the oxygen and carbon isotope compositions of the skarn calcites (Fig. 11) are also consistent with the presence of a magmatic hydrothermal fluid during the skarn formation. As mentioned earlier, changes in temperature and/or fO_2 and pH conditions are insufficient to explain the isotopic composition of the sulfides deposited during the second stage. Thus, a second contribution of sulfur, with a heavier isotopic composition with respect to the first magmatic one, is necessary. In this case, we propose that leaching of the surrounding host rocks provided sulfur for the fluid system.

8.4. Metallogenic model

The mineralization of the Vilalba gold district shares many similarities with the intrusion related gold systems, IRGSs, (Baker and Lang, 2001; Hart, 2007; Hart et al., 2000; Lang and Baker, 2001; Lang et al., 2000; Thompson et al., 1999). These systems include a wide variety of hydrothermal mineral deposits developed at the contact or in the proximity of igneous bodies. The related igneous rocks are mainly intermediate to felsic metaluminous and subalcaline, although peraluminous intrusions such as those observed in the Vilalba gold district are also usually present (Coulson et al., 2001; Gordey and Anderson, 1993; Hart, 2007). Contact aureole including calc-silicate and biotite-hornfels, similar to those developed in the Castro de Rei area, are associated with the igneous rocks of the IRGS.

Mineral deposits in IRGS span a broad range of style, metal signature and position relative to intrusive centers. The mineral deposits developed over a broad range of depth (in excess of 6 Km, Lang et al., 2000) and maximum lateral extension of 3 km from the intrusion center. Deposits within or immediately adjacent to the intrusion have a characteristic Au–Bi–W ± Te ± Mo ± As metal signature, whereas deposits peripheral to intrusions are characterized by Au–As–Sb–Hg–Ag–Pb–Zn metal signature.

In the IRGS, deposits such as Fort Knox, in Alaska (Bakke, 1995), and the recently defined Linares in the northwest of Spain (Cepedal et al., 2013) are *intrusion-hosted* gold deposits consisting of sheeted veins and more rarely stockwork veins with a metallic association of Au–Bi–W ± Te ± Mo ± As. Skarns of tungsten, such as Mactung (Bowman, 1998) or Ray Gulch (Brown et al., 2001), in the Tintina gold belt, are included within the *Proximal Deposit Styles* (Lang and Bakker, 2001), which are located in host rocks adjacent to or slightly removed from the intrusions, but within the metamorphic aureole. These skarn deposits are typically reduced and show a metallic association of W–Bi ± Au–Cu–Mo, similar to that observed in the Castro de Rei skarn.

The polymetallic mineralization of Valiña–Azúmara and Arcos can be included within the *Distal Deposit Style* (Lang and Bakker, 2001). In the IRGS, distal deposits are located beyond the outer limit of the hornfels. They include auriferous, mesothermal to epithermal quartz–sulfide veins along steep faults (e.g. Donlin Creek, Alaska, Ebert et al., 2000), hydrothermal breccias and base-metal veins enriched in Ag ± Au, and gold disseminations in calcareous and carbonaceous sedimentary rocks similar to those of the Carlin-type deposits (Lang and Baker, 2001). The metallic association Ag–Pb–Zn–(Au) is generally located in distal veins, but also represents the latter stage of mineralization (Lang et al., 2000).

With respect to the fluid inclusion and stable isotope data, the mineralized areas of the Vilalba gold district also share many of the recurrent characteristics indicated by Lang and Baker (2001) and Baker and Lang (2001) for the IRGS. Thus, the CO_2-rich fluids are almost ubiquitous and there is a common pattern of early carbonic fluids of low salinity evolving to later aqueous fluids of low to moderate salinity. Furthermore, other components, such as CH_4 and N_2, observed in most of the aqueous-carbonic fluids of the district, are abundant in the intrusion-hosted deposits formed at higher pressures (>1.5 kbar) and in the proximal and distal deposits of the IRGS. According to these authors, the locally elevated CH_4 and N_2 may have derived from deep crustal contamination, a mantle source or, alternatively, a fluid derived from the host-rock. As previously noted, the results of the isotope and fluid inclusion study suggest that the presence of CH_4 and N_2 in the aqueous-carbonic fluids from the district is due to the influence of metamorphosed carbonaceous host-rocks from the Limestone and Slate Fm. Moreover, according to Baker and Lang (2001), although the fluids responsible for intrusion-hosted ores in the IRGS are predominantly magmatic in origin, with little or no influence from metamorphic or meteoric fluids, the relative importance of these three fluid types becomes less clear with increasing distance from the intrusion.

Furthermore, temperatures and pressures attending precipitation of gold and related metals in the Vilalba gold district are within the ranges of <200 to >600 °C and >0.5 to >3.0 kbar proposed for the IRGS. In the case of the Castro de Rei skarn, the gold mineralization is related to the second stage of mineralization and the estimated temperatures range between 285 and 388 °C for an interval of pressures of between

Please cite this article as: Martínez-Abad, I., et al., The Vilalba gold district, a new discovery in the Variscan terranes of the NW of Spain: A geologic, fluid inclusion and stable isotope study, Ore Geol. Rev. (2014), http://dx.doi.org/10.1016/j.oregeorev.2014.10.021

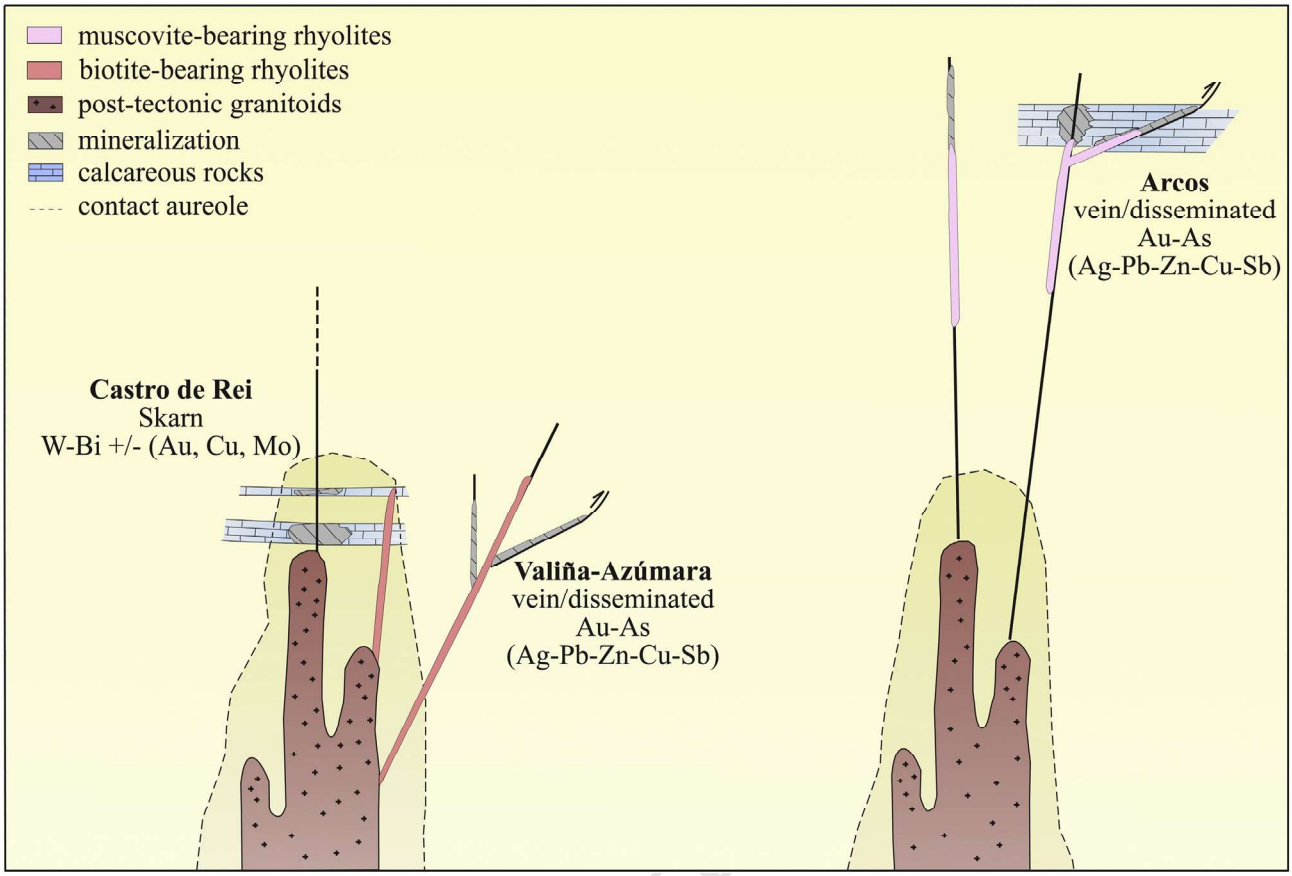

Fig. 16. Squematic geological and exploration model for the ore deposits that constitutes the Vilalba gold district.

1.3 and 2.1 kbar. The P–T conditions of gold precipitation established in Valiña–Azúmara are over 355 °C and pressures around 1.7 kbar. In the case of Arcos, gold mineralization was identified in both the first and the second stage of mineralization. Although we have not obtained enough data to constrain the P–T conditions of formation for the deposit, the arsenopyrite geothermometer and fluid inclusion study show that gold precipitation took place at temperatures ranging from 186 and 383 °C.

Considering the geological and exploration model proposed for the IRGS (Lang and Baker, 2001; Lang et al., 2000), the maximum lateral extension of the systems can attain from the intrusion center and the situation of the igneous rocks within the district, and two independent IRGS can be distinguished within the Vilalba gold district (Fig. 16). One would comprise the Castro de Rei skarn and the mineralized area of Valiña–Azúmara (Au–As + Ag–Pb–Zn–Cu–Sb). While the skarn is interpreted as a proximal deposit to an unexposed post-tectonic granitoid located at depth, the mineralization of Valiña–Azúmara is interpreted as a distal deposit to the igneous rock. Taking into account the estimated maximum pressures of emplacement for the post-tectonic granitoids of the Lugo Dome (2 kbar) and the range of pressures obtained for the different stages of mineralization in Castro de Rei and Valiña–Azúmara, we assume that both mineralization were situated at maximum pressures of around 1.7 to 2 kbar (~9 km depth) at the moment of their formation. The other IRGS would comprise the mineralized area of Arcos, which has been interpreted as a distal deposit related to an unexposed post-tectonic granitoid situated at depth. As previously mentioned, the homogenization pressures obtained in Arcos are always lower compared to the mineralized areas of Castro de Rei and Valiña–Azúmara. So we assume that the Arcos deposit was in a shallower emplacement at the moment of its formation.

IRGSs have achieved recognition as a different style of gold mineralization with significant gold endowment (i.e. multi-million oz deposits). The analogies of the Vilalba gold district with IRGS encourage exploration in other post-tectonic granitoids of the Lugo Dome as well as in other gold regions of the NW of the Iberian Peninsula.

9. Uncited references

Arcos et al., 1995
Boiron et al., 2003
Cepedal et al., 2008
Fuertes-Fuentes et al., 2000
Schulz, 1835

Acknowledgments

The authors wish to thank Outokumptu S.A and RNGM for the data provided. This work has been financed by the Science and Innovation Ministry of Spain projects CGL2007-62298 and CGL2011-2319, and supported by FPI of the Educational Sciences Ministry of Spain grant to Martínez-Abad. The authors also wish to thank James K. Mortensen and another anonymous reviewer, as well as chief editor Franco Pirajno, for their constructive comments and suggestions that greatly improved this manuscript.

References

Ancochea, E., Huertas Coronel, M.J., Ibarrola, E., Snelling, E., 1992. Diques basálticos en las proximidades de Orense. Evidencia de actividad magmática cretácica en el noroeste de la Península Ibérica. Rev. Soc. Geol. Esp. 5 (3–4), 65–71.
Arcos, D., Soler, A., Delgado, J., 1995. Gold–copper deposit related with the Carlés granodiorite (NW Spain). In: Pasava, J., Kribek, B., Zak, K. (Eds.), Mineral Deposits: From Their Origin to Environmental Impacts. Balkema, Rotterdam, pp. 411–414.
Arias, D., Corretgé, L.G., Villa, L., Gallastegui, G., Suárez, O., Cuesta, A., 1997. A sulfur isotopic study of the Navia gold belt (Spain). J. Geochem. Explor. 59, 1–10.

Please cite this article as: Martínez-Abad, I., et al., The Vilalba gold district, a new discovery in the Variscan terranes of the NW of Spain: A geologic, fluid inclusion and stable isotope study, Ore Geol. Rev. (2014), http://dx.doi.org/10.1016/j.oregeorev.2014.10.021

Ayora, C., Ribera, F., Cardellach, E., 1992. The genesis of the arsenopyrite gold veins from the Vall de Ribes District, eastern Pyrenees, Spain. Econ. Geol. 87, 1877–1896.
Baker, T., Lang, J.R., 2001. Fluid inclusion characteristics of intrusion-related gold mineralization, Tombstone–Tungsten magmatic belt, Yukon Territory, Canada. Mineral. Deposita 36, 563–582.
Bakke, A.A., 1995. The Fort knox "porphyry" gold deposit structurally-controlled stockwork and shear quartz vein, sulfide-poor mineralization hosted by a Late Cretaceous pluton, east-central Alaska. Porphyry Deposits of Northwestern Cordillera of North America. Canadian Institute of Mining and Metallurgy.
Bakker, R.J., 1997. Clathrates: computer programs to calculate fluid inclusion V–X properties using clathrate melting temperatures. Comput. Geosci. 23, 1–18.
Bakker, R.J., 2003. Package FLUIDS 1 computer programs for analysis of fluid inclusion data and for modeling bulk fluid properties. Chem. Geol. 194, 3–23.
Bakker, R.J., Brown, P., 2003. Computer modelling in fluid inclusion research. In: Samson, I., Anderson, A., Marshall, D. (Eds.), Fluid Inclusions: Analysis and Interpretation: Mineralogical Association of Canada. Short Course 32, pp. 175–212.
Bastida, F., Martínez Catalán, J.R., Pulgar, J.A., 1986. Structural, metamorphic and magmatic history of the Mondoñedo nappe (Hercynian belt, NW Spain). J. Struct. Geol. 8, 415–430.
Bebout, G.E., Cooper, D.C., Bradley, A.D., Sadofsky, S.J., 1999. Nitrogen-isotope record of fluid–rock interactions in the Skiddaw aureole and granite, English Lake District. Am. Mineral. 84, 1495–1505.
Bellido Mulas, F., González-Lodeiro, F., Klein, E., Martínez Catalán, J.R., Pablo Macia, J.G., 1987. Las rocas graníticas hercínicas del norte de Galicia y occidente de Asturias. Memoria del IGME.
Boiron, M.C., Cathelineau, M., Banks, D.A., Yardley, B.W.D., Noronha, F., Miller, M.F., 1996. P–T–X conditions of late Hercynian fluid penetration and the origin of granite hosted gold quartz veins in northwestern Iberia: a multidisciplinary study of fluid inclusions and their chemistry. Geochim. Cosmochim. Acta 60, 43–57.
Boiron, M.C., Cathelineau, M., Banks, D.A., Fourcade, S., Vallance, J., 2003. Mixing of metamorphic and surficial fluids during the uplift of the Hercynian upper crust: consequences for gold deposition. Chem. Geol. 194, 119–141.
Boixet, L., Gleeson, C.F., García, J., 2007. The Corcoesto gold-deposit. 23rd International Applied Geochemistry Symposium (IAGS 2007). Congress Proceedings of Oviedo.
Bottinga, Y., Javoy, M., 1973. Comments on oxygen isotope geothermometry. Earth Planet. Sci. Lett. 20, 250–265.
Bottinga, Y., Javoy, M., 1975. Oxygen isotope partitioning among the minerals in igneous and metamorphic rocks. Rev. Geophys. Space Phys. 13, 401–418.
Bowman, J.R., 1998. Stable-isotope systematics of skarns Mineralogical Association of Canada. Short Course Ser. 26, 99–145.
Bowman, J.R., Covert, J.J., Clarck, A.H., Mathieson, G.A., 1985. The Cantung E-zone scheelite skarn orebody, Tungsten, Northwest Territories, Canada: oxygen, hydrogen, and carbon isotope studies. Econ. Geol. 80, 1872–1875.
Brown, V.S., Baker, T., Stephens, J.R., 2001. Ray Gulch tungsten skarn, Dublin Gulch, central Yukon: gold–tungsten relationships in intrusion-related ore systems and implications for gold exploration. Yukon Explor. Geol. 259–268.
Burrus, R.C., 1981. Analysis of fluid inclusions: phase equilibria at constant volume. Am. J. Sci. 281, 1104–1126.
Capdevila, R., 1969. Le métamorphisme régional progressif et les granites dans le segment hercynien de Galice Nord orientale (NW de l'Espagne)(PhD Thesis) University of Montpellier, (430 pp.).
Capdevila, R., Corretge, G., Floor, P., 1973. Les granitoides varisques de la Meseta Ibérique. Bull. Soc. Geol. Fr. 3–4, 209–228.
Capote, R., 1983. La fracturación subsecuente a la orogenia varisca. Libro Jubilar J. M. Ríos. Geología de España, II. IGME, pp. 17–24.
Cathelineau, M., 1988. Cation site occupancy in chlorites and illites as a function of temperature. Clay Miner. 23, 471–485.
Cathelineau, M., Boiron, M.C., Essarraj, S., Dubessy, J., Lespinasse, M., Poty, B., 1993. Fluid pressure variations in relation to multistage deformation and uplift: a fluid inclusion study of Au quartz veins. Eur. J. Mineral. 5, 107–121.
Cepedal, A., 2001. Geología, mineralogía, evolución y modelo genético del yacimiento de Au–Cu de "El Valle-Boinás", Belmonte (Asturias)(PhD Thesis) University of Oviedo, (ISBN: 978-84-8317-737-2).
Cepedal, A., Martín-Izard, A., Reguilón, R., Rodríguez-Pevida, L., Spiering, E., González Nistal, S., 2000. Origin and evolution of the calcic and magnesian skarns hosting the El Valle–Boinás copper–gold deposit, Asturias (Spain). J. Geochem. Explor. 71, 119–151.
Cepedal, A., Fuertes-Fuente, M., Martin-Izard, A., Boiron, M.C., 2003. Fluid composition in Ortosa Au-skarn and El Valle-Boinás Cu–Au skarn, Río Narcea Gold Belt (Spain). Acta Mineral. Petrogr. Abstr. Ser. Szeged. 2, 36–37.
Cepedal, A., Fuertes-Fuente, M., Martin-Izard, A., Gonzalez Nistal, S., Barrero, M., 2008. Gold-bearing As-rich pyrite and arsenopyrite from the El Valle gold deposit, Asturias, northwestern Spain. Can. Mineral. 46, 233–247.
Cepedal, A., Fuertes-Fuente, M., Martín-Izard, A., García-Nieto, J., Boiron, M.C., 2013. An intrusion-related gold deposit (IRGD) in the NW of Spain, the Linares deposit: igneous rocks, veins and related alterations, ore features and fluids involved. J. Geochem. Explor. 124, 101–126.
Champion, D.C., Chappell, B.W., 1992. Petrogenesis of felsic I-type granites: an example from northern Queensland. Trans. R. Soc. Edinb. Earth Sci. 83 (1–2), 115–126.
Claypool, G.W., Holser, W.T., Kaplan, I.R., Sakai, H., Zak, I., 1980. The age curves of sulfur and oxygen isotopes in marine sulfate and their mutual interpretation. Chem. Geol. 28, 199–260.
Cocherie, A., Albarede, F., 2001. An improved U–Th–Pb age calculation for electron microprobe dating of monazite. Geochim. Cosmochim. Acta 65 (24), 4509–4522.
Corretgé, G., Suárez, O., 1990. Cantabrian zone: igneous rock. In: Dallmeyer, R.D., Martínez García, E. (Eds.), Pre-Mesozoic Geology of Iberia. Springer-Verlag, Berlín, pp. 72–80.
Corretgé, L.G., Suárez, O., Galán, G., 1990. West Asturian–Leonese Zone: igneous rocks. In: Dallmeyer, R.D., Martínez García, E. (Eds.), Pre-Mesozoic Geology of Iberia. Springer-Verlag, Berlín, pp. 115–128.
Corretgé, L.G., Suárez, O., Galán, G., Fernández-Suárez, J., 2004. Magmatismo de la Zona Asturoccidental-leonesa. In: Vera, J.A. (Ed.), Geología de España. SGE-IGME, Madrid, pp. 63–68.
Coulson, I.M., Dipple, G.M., Raudsepp, M., 2001. Evolution of HF and HCl activity in magmatic volatiles of the gold mineralized Emerald Lake pluton, Yukon Territory, Canada. Mineral. Deposita 36, 594–606.
Craig, H., 1961. Standard for reporting concentrations of deuterium and oxygen-18 in natural waters. Science 133, 1833–1834.
Crespo, J.L., Moro, M.C., Fadón, O., Cabrera, R., Fernández, A., 2000. The Salamón gold deposit (León, Spain). J. Geochem. Explor. 71, 191–208.
Dallmeyer, R.D., Martínez Catalán, J.R., Arenas, R., Gil Ibarguchi, J.I., Gutiérrez Alonso, G., Farias, P., Bastida, F., Aller, J., 1997. Diachronous Variscan tectonothermal activity in the NW Iberian Massif: evidence from $^{40}Ar/^{39}Ar$ dating of regional fabrics. Tectonophysics 277, 307–337.
Douglas, N., Mavrogenes, J., Hack, A., England, R., 2000. The liquid bismuth collector model: an alternative gold deposition mechanism. In: Silbeck, G., Hubble, T.C.T. (Eds.), Understanding Planet Earth; Searching for a Sustainable Future on the Starting Blocks of the Third Millennium. 15th Australian Geological Convention Abstracts. Geological Society of Australia, Sydney (135 pp.).
Dubessy, J., 1984. Simulation des équilibres chimiques dans le système C–O–H Conséquences méthodologiques pour les inclusions fluides. Bull. Mineral. 107, 157–768.
Dubessy, J., Poty, B., Ramboz, C., 1989. Advances in the C–O–H–N–S fluid geochemistry based on micro-Raman spectroscopic analysis of fluid inclusions. Eur. J. Mineral. 1, 517–534.
Ebert, S., Miller, L., Petsel, S., Dodd, S., Kowalczyk, P., 2000. Geology, mineralization, and exploration at the Donlin Creek project, southwestern Alaska. The Tintina Gold Belt: concepts, exploration and discoveries British Columbia and Yukon Chamber of Mines. Special 2, 99–114.
Farias, P., Gallastegui, G., González-Lodeiro, F., Marquínez, J., Martín Parra, L., Martínez Catalán, J.R., De Pablo Maciá, J.G., Rodríguez Fernández, L.R., 1987. Aportaciones al conocimiento de la litoestratigrafía y estructura de Galicia Central. Faculdade de Ciências do Porto. Mem. Museu Laboratório Mineralógico Geol. 1, 411–431.
Fernández-Catuxo, J., 1998. The Salave Gold Prospect revisited: new ideas for an old deposit. In: Arias, D., Martín-Izard, A., Paniagua, A. (Eds.), Gold Exploration and Mining in NW SpainInternational Meeting of Gold Exploration and Mining in NW Spain. Oviedo, Spain, pp. 82–85.
Fernández-González, M., Cuesta, A., Rubio-Ordóñez, A., Valverde-Vaquero, P., 2009. Datación química U–Th–Pb de monacita por microsonda electrónica (CHIME-EPMA Dating): Puesta a punto y resultados. VII Congreso Ibérico; X Congreso Nacional de Geoquímica Diputación de Soria, pp. 170–177.
Fernández-Suárez, J., Dunning, G.R., Jenner, G.A., Gutiérrez-Alonso, G., 2000. Variscan collisional magmatism and deformation in NW Iberia: constrains from U–Pb geocronology of granitoids. J. Geol. Soc. 157, 565–576.
Foerster, H.J., 1998. The chemical composition of REE–Y–Th–U-rich accessory minerals in peraluminous granites of the Erzgebirge–Fichtelgebirge region, Germany; part I, the monazite–(Ce)–brabantite solid solution series. Am. Mineral. 83 (3–4), 259–272.
Fuertes-Fuentes, M., Martín-Izard, A., Nieto, J.G., Maldonado, C., Varela, A., 2000. Preliminary mineralogical and petrological study of the Ortosa Au–Bi–Te ore deposit: a reduced gold skarn in the northern part of the Rio Narcea Gold Belt, Asturias, Spain. J. Geochem. Explor. 7, 177–190.
Gerstner, M.R., Bowman, J.R., Pasteris, J.D., 1989. Skarn formation at the MacMillan Pass tungsten deposit (MacTung), Yukon and Northwest Territories: I. P–T–X–V characterization of the methane-bearing, skarn-forming fluids. Can. Mineral. 27, 545–563.
Gómez-Fernández, F., Vindel, E., Martín-Crespo, T., Sánchez, V., González Clavijo, E., Matías, R., 2012. The Llamas de Cabrera gold district, a new discovery in the Variscan basement of northwest Spain: a fluid inclusion and stable isotope study. Ore Geol. Rev. 46, 68–82.
González Lodeiro, F., Martínez Catalán, J.R., Pablo Macia, J.G., Pérez González, A., 1979. Mapa geológico de España 1:50.000. Meira (58). I.G.M.E.
González Lodeiro F., Hernández Urroz, J., Klein, E., Martínez Catalán, J.R., Pablo Macia, J.G., 1982. Mapa geológico de España 1:200.000. Lugo (8). I.G.M.E.
Gordey, S.P., Anderson, R.G., 1993. Evolution of the northern Cordilleran miogeocline, Nahanni map area (105I), Yukon and Northwest Territories. Geological Survey of Canada, Memoir 428. 214 pp.
Gumiel, P., Martín-Izard, A., Arias, M., Rodríguez-Terente, L., 2008. Geometrical analysis of the Punta del Pedrón shear zone (Asturias, Spain): Implications related to exploration of Salave Gold-type mineralization. J. Struct. Geol. 30 (3), 354–365.
Gutiérrez Claverol, M., Martínez-García, E., Luque, C., Suárez, V., Ruiz, F., 1991. Gold deposits, late Hercynian tectonics and magmatism in the northeastern Iberian Massif (NW Spain). Chron. Rech. Min. 503, 3–13.
Gutiérrez-Alonso, G., Fernández-Suárez, J., Jeffries, T.E., Johnston, S.T., Pastor-Galán, D., Murphy, J.B., Franco, M.P., Gonzalo, J.C., 2011. Diachronous post-orogenic magmatism within a developing orocline in Iberia, European Variscides. Tectonics 30, 1–17.
Harris, M., 1980a. Gold mineralization at the Salave gold prospect, northwest Spain. Trans. Inst. Min. Metall. Sect. B 89, 1–4.
Harris, M., 1980b. Hydrothermal alteration at the Salave gold prospect, northwest Spain. Trans. Inst. Min. Metall., Sect. B-Appl. Earth Sci. 89 (FEB), B5–B15.
Hart, C.J.R., 2007. Reduced intrusion-related gold deposits. In: Goodfellow, W.D. (Ed.), Mineral Deposits of Canada: Geological Association of Canada, Special, Publication 5, pp. 95–112.
Hart, C.J.R., Baker, T., Burke, M., 2000. New exploration concepts for country-rock-hosted, intrusion-related gold systems: Tintina gold belt in Yukon. In: Tucker, T.L., Smith, M.T. (Eds.), The Tintina Gold Belt: Concepts, Exploration and Discoveries. British Columbia and Yukon Chamber of Mines Special volume 2, pp. 145–172.

Please cite this article as: Martínez-Abad, I., et al., The Vilalba gold district, a new discovery in the Variscan terranes of the NW of Spain: A geologic, fluid inclusion and stable isotope study, Ore Geol. Rev. (2014), http://dx.doi.org/10.1016/j.oregeorev.2014.10.021

Hofstra, A.H., Cline, J.S., 2000. Characteristics and models for Carlin-type gold deposits. Rev. Econ. Geol. 13, 163–220.
Julivert, M., Fontboté, J.M., Ribeiro, A., Nabais Conde, L.E., 1972. Mapa Tectónico de la Península Ibérica y Baleares. Scale 1:1.000.000. IGME.
Kranidiotis, P., MacLean, W.H., 1987. Systematics of chlorite alteration at the Phelps Dodge massive sulfide deposit, Matagami, Quebec. Econ. Geol. 82, 1898–1911.
Kretschmar, U., Scott, S., 1976. Phase relations involving arsenopyrite in the system Fe–As–S and their application. Can. Mineral. 14, 364–386.
Lang, J.R., Baker, T., 2001. Intrusion-related gold systems: the present level of understanding. Mineral. Deposita 36, 477–489.
Lang, J.R., Baker, T., Hart, C.J.R., Mortensen, J.K., 2000. An exploration model for intrusion-related gold systems. Soc. Econ. Geol. Newsl. 40 (1), 6–15.
Le Maitre, R., Bateman, P., Dudek, A., Keller, J., Lameyre, J., Le Bas, M., Sabine, P., Schmid, R., Sorensen, H., Streckeisen, A., Woolley, A., Zanettin, B., 1989. In: Le Maitre, R.W. (Ed.), A Classification of Igneous Rocks and Glossary of Terms: Recommendations of the International Union of Geological Sciences Subcommission on the Systematics of Igneous Rocks. Blackwell, Oxford (193 pp.).
Ludwig, K.R., 2003. Isoplot/Ex. version 3.00.
Martínez-Abad, I., Cepedal, M.A., Arias, D., Martín-Izard, A., 2011a. The Vilalba Gold District, NW Spain. In: Barra, E., Reich, M., Campos, E., Tornos, F. (Eds.), Let's Talk Ore Deposits. Ediciones Universidad Católica del Norte, Antofagasta, Chile, pp. 550–552.
Martínez-Abad, I., Cepedal, M.A., Arias, D., Martín-Izard, A., Roberts, S., 2011b. Invisible gold at the Arcos deposit (Lugo, NW of Spain). In: Barra, E., Reich, M., Campos, E., Tornos, F. (Eds.), Let's Talk Ore Deposits. Ediciones Universidad Católica del Norte, Antofagasta, Chile, pp. 553–555.
Martínez-Catalán, J.R., Pérez-Estaún, A., Bastida, F., Pulgar, J.A., Marcos, A., 1990. West Asturian–Leonese Zone: structure. In: Dallmeyer, R.D., Martínez-García, E. (Eds.), Pre-mesozoic Geology of Iberia, pp. 103–114.
Martín-Izard, A., Paniagua, A., García-Iglesias, J., Fuertes-Fuente, M., Boixet, Ll, Maldonado, C., Varela, A., 2000a. The Carlés copper–gold–molybdenum skarn (Asturias, Spain): geometry, mineral associations and metasomatic evolution. J. Geochem. Explor. 71, 153–175.
Martín-Izard, A., Fuertes-Fuente, M., Cepedal, A., Moreiras, D., Nieto, J.G., Maldonado, C., Pevida, L.R., 2000b. The Río Narcea Gold Belt Intrusions: geology, petrology, geochemistry and timing. J. Geochem. Explor. 71, 103–117.
Martín-Izard, A., Gumiel, P., Arias, M., Cepedal, A., Fuertes-Fuente, M., Reguilón, R., 2009. Genesis and evolution of the structurally controlled vein mineralization (Sb–Hg) in the Escarlati deposit (León, Spain): evidence from fault population analysis methods, fluid-inclusion research and stable isotope data. J. Geochem. Explor. 100, 51–66.
Montel, J.M., Foret, S., Veschambre, M., Nicollet, C., Provost, A., 1996. Electron microprobe dating of monazite. Chem. Geol. 131 (1–4), 37–53.
Murowchick, J.B., 1992. Marcasite inversion and the petrographic recognition of pyrite ancestry. Econ. Geol. 87, 1141–1152.
Newberry, R.J., 1983. The formation of subcalcic garnet in scheelite-bearing skarns. Can. Mineral. 21, 529–544.
Ohmoto, H., 1972. Systematics of sulphur and carbon isotopes in hydrothermal ore deposits. Econ. Geol. 67, 551–578.
Ohmoto, H., Rye, R.O., 1979. Isotope of sulfur and carbon. In: Barnes,, H.Ll (Ed.), Geochemistry of Hydrothermal Deposits. John Wiley & Sons, pp. 509–567.
Okamoto, K., Tanner, L.E., 1990. Bi–Te (bismuth–tellurium). In: Massalski, T.B., Okamoto, K. (Eds.), Binary Alloy Phase Diagrams. ASM International, Materials Park, Ohio, Ohio, pp. 800–801.
Pérez-Estaún, A., Bastida, F., Martínez Catalán, J.R., GutiérrezMarco, J.C., Marcos, A., Pulgar, J.A., 1990. West Asturian–Leonese zone, stratigraphy. In: Dallmeyer, R.D., Martínez-García, E. (Eds.), Pre-Mesozoic Geology of Iberia. Springer-Verlag, Berlin, pp. 92–102.
Potter, R.W., Brown, D.L., 1977. The volumetric properties of aqueous sodium chloride solution from 0 °C to 500 °C at pressures up to 2000 bars based on a regression of available data in the literature. U.S. Geol. Surv. Bull. 1421-C, C1–C36.
Ribera, F., Tornos, F., Locutura, J., 1992. Las mineralizaciones hidrotermales de oro de la vertiente norte del Teleno (León). III Congreso Geológico de España 3, pp. 418–421.
Rickwood, P.C., 1989. Boundary lines within petrologic diagrams which use oxides of major and minor elements. Lithos 22, 247–263.
Rodríguez-Terente, L.M., 2007. Las mineralizaciones auríferas de la granodiorita de Salave (Tapia de Casariego, Asturias)(PhD Thesis) University of Oviedo.
Roedder, E., 1984. Fluid inclusions. Reviews in Mineralogy. Mineral Society of America, Washington DC, p. 12.
Scherrer, N.C., Engi, M., Gnos, E., Jakob, V., Liechti, A., 2000. Monazite analysis; from sample preparation to microprobe age dating and REE quantification. Schweiz. Mineral. Petrogr. Mitt. 80 (1), 93–105.
Schulz, G., 1835. Descripción geognóstica del Reino de Galicia. Imprenta de los Herederos de Collado.
Sharp, D., Essene, J., Kelly, C., 1985. A re-examination of the arsenopyrite geothermometer: pressure considerations and applications to natural assemblages. Can. Mineral. 23, 517–534.
Shepherd, T.J., Rankin, A.H., Alderton, D.H.M., 1985. A Practical Guide to Fluid Inclusion Studies. Blackie, Glasgow.
Spiering, E.D., Pevida, L.R., Maldonado, C., González, S., García, J., Varela, A., Arias, D., Martín-Izard, A., 2000. The gold belts of Western Asturias and Galicia (NW Spain). J. Geochem. Explor. 71, 89–101.
Suárez, O., Corretgé, L.G., Martínez, F.J., 1990. West Asturian–Leonese Zone. Distribution and characteristics of the Hercynian metamorphism. In: Dallmeyer, R.D., Martínez García, E. (Eds.), Pre-Mesozoic Geology of Iberia. Springer-Verlag, Berlin, pp. 129–133.
Suzuki, K., Adachi, M., 1991. The chemical Th–U-Total Pb isochron ages of zircon and monazite from the Gray Granite of the Hida Terrane, Japan. J. Earth Sci. Nagoya Univ. 38, 11–38.
Taylor, S.R., McLennan, S.H., 1985. The Continental Crust: Its Composition and Evolution. Blackwell, Oxford, p. 312.
Thiery, R., Vidal, J., Dubessy, J., 1994. Phase equilibria modeling applied to fluid inclusions liquid vapour equilibria and calculation of the molar volume in the CO_2–CH_4–N_2 system. Geochim. Cosmochim. Acta 58, 1073–1082.
Thompson, J.F.H., Sillitoe, R.H., Baker, T., Lang, J.R., Mortensen, J.K., 1999. Intrusion related gold deposits associated with tungsten–tin provinces. Mineral. Deposita 34, 197–217.
Tooth, B., Brugger, J., Ciobanu, C., Liu, W., 2008. Modeling of gold scavenging by bismuth melts coexisting with hydrothermal fluids. Geology 36, 815–818.
Tooth, B., Ciobanu, C.L., Green, L., O'Neill, B., Brugger, J., 2011. Bi melt formation and gold scavenging from hydrothermal fluids: an experimental study. Geochim. Cosmochim. Acta 75, 5423–5443.
Tornos, F., Arias, D., 1993. Sulfur and lead isotope geochemistry of the Rubiales Zn–Pb ore deposit (NW Spain). Eur. J. Mineral. 5, 763–773.
Tornos, F., Ribera, F., Sheperd, T.J., Spiro, B., 1996. The geological and metallogenic setting of stratabound carbonate-hosted Zn–Pb mineralizations in the West Asturian Leonese Zone, NW Spain. Mineral. Deposita 31, 27–40.
Valverde-Vaquero, P., Vallaure, A.M., Arquer, P.F., Suárez, G.M.G., 2005. U–Pb dating of Ordovician felsic volcanism in the schistose domain of the Galicia-Trás-os-Montes Zone near Cabo Ortegal (NW Spain). Geol. Acta 3 (1), 27.
Veizer, J., Hoefs, J., 1976. The nature of $^{18}O/^{16}O$ and $^{13}C/^{12}C$ secular trends in sedimentary carbonate rocks. Geochem. Cosm. Ac. 40, 1387–1395.
Villaseca, C., Pérez-Soba, C., González del Tánago, J., 2004. Evolución contrastada de elementos trazas (Th–U–Y–HREE) entre granitos fraccionados de tipo-I y tipo-S de la Sierra de Guadarrama: reflejo en la química de minerales accesorios. Geotemas 6 (1), 141–144.
Walter, R., 1966. Resultados de las investigaciones geológicas en el Noroeste de la Provincia de Lugo (NO de España). Notas y comunicaciones del IGME 89, 7–16.
Williams, M.L., Jercinovic, M.J., Terry, M.P., 1999. Age mapping and dating of monazite on the electron microprobe: deconvoluting multistage tectonic histories. Geology 27 (11), 1023–1026.
Winkler, H.G.F., 1979. Petrogenesis of Metamorphic Rocks, 5 ed. Springer-Verlag, New York.
Xie, X., Byerly, G.R., Ferrell Jr., R.E., 1997. IIb trioctahedral chlorite from the Barberton greenstone belt: crystal structure and rock composition constraints with implications to geothermometry. Contrib. Mineral. Petrol. 126 (3), 275–291.
Zheng, Y.F., 1993. Calculation of oxygen isotope fractionation in anhydrous silicate minerals. Geochim. Cosmochim. Acta 57, 1079–1091.
Zheng, Y.F., 1999. Oxygen isotope fractionation in carbonate and sulfate minerals. Geochem. J. 33, 109–126.

Please cite this article as: Martínez-Abad, I., et al., The Vilalba gold district, a new discovery in the Variscan terranes of the NW of Spain: A geologic, fluid inclusion and stable isotope study, Ore Geol. Rev. (2014), http://dx.doi.org/10.1016/j.oregeorev.2014.10.021